



**HAL**  
open science

## Subducted oceanic relief locks the shallow megathrust in central Ecuador

Jean-Yves Collot, Eddy Sanclemente, Jean-Mathieu Nocquet, Angélique Leprêtre, Alessandra Ribodetti, Paul Jarrin, Mohamed Chlieh, David Graindorge, Philippe Charvis

### ► To cite this version:

Jean-Yves Collot, Eddy Sanclemente, Jean-Mathieu Nocquet, Angélique Leprêtre, Alessandra Ribodetti, et al.. Subducted oceanic relief locks the shallow megathrust in central Ecuador. *Journal of Geophysical Research: Solid Earth*, 2017, 122 (5), pp.3286 - 3305. 10.1002/2016JB013849 . hal-01734549

**HAL Id: hal-01734549**

**<https://hal.science/hal-01734549>**

Submitted on 9 Apr 2021

**HAL** is a multi-disciplinary open access archive for the deposit and dissemination of scientific research documents, whether they are published or not. The documents may come from teaching and research institutions in France or abroad, or from public or private research centers.

L'archive ouverte pluridisciplinaire **HAL**, est destinée au dépôt et à la diffusion de documents scientifiques de niveau recherche, publiés ou non, émanant des établissements d'enseignement et de recherche français ou étrangers, des laboratoires publics ou privés.

## RESEARCH ARTICLE

10.1002/2016JB013849

## Key Points:

- Seismic imaging and geodetic data show a shallow subducted oceanic relief to lock the plate interface
- The jagged oceanic relief topography hosts regular slow slip events and seismic swarms occurring within the locked patch
- The subducted oceanic relief undergoes internal shearing and produces margin deformation including La Plata Island uplift

## Supporting Information:

- Supporting Information S1

## Correspondence to:

J.-Y. Collot,  
jean-yves.collot@ird.fr

## Citation:

Collot, J.-Y., E. Sanclemente, J.-M. Nocquet, A. Leprêtre, A. Ribodetti, P. Jarrin, M. Chlieh, D. Graindorge, and P. Charvis (2017), Subducted oceanic relief locks the shallow megathrust in central Ecuador, *J. Geophys. Res. Solid Earth*, 122, 3286–3305, doi:10.1002/2016JB013849.

Received 11 DEC 2016

Accepted 16 APR 2017

Accepted article online 20 APR 2017

Published online 13 MAY 2017

## Subducted oceanic relief locks the shallow megathrust in central Ecuador

Jean-Yves Collot<sup>1,2,3</sup> , Eddy Sanclemente<sup>1,4</sup>, Jean-Mathieu Nocquet<sup>1,2</sup> , Angélique Leprêtre<sup>1</sup>, Alessandra Ribodetti<sup>1</sup> , Paul Jarrin<sup>2</sup>, Mohamed Chlieh<sup>1</sup> , David Graindorge<sup>5</sup>, and Philippe Charvis<sup>1</sup> 

<sup>1</sup>Université Côte d'Azur, IRD, CNRS, OCA, Géoazur, Valbonne, France, <sup>2</sup>Instituto Geofísico, Escuela Politécnica Nacional, Quito, Ecuador, <sup>3</sup>Investigator of the Prometeo Project of the Ministry of Higher Education, Science, Technology and Innovation of the Republic of Ecuador, Ecuador, <sup>4</sup>Escuela Superior Politécnica del Litoral, Guayaquil, Ecuador, <sup>5</sup>Laboratoire Domaines Océaniques, Université de Bretagne Occidentale, Plouzane, France

**Abstract** Whether subducted oceanic reliefs such as seamounts promote seismic rupture or aseismic slip remains controversial. Here we use swath bathymetry, prestack depth-migrated multichannel seismic reflection lines, and wide-angle seismic data collected across the central Ecuador subduction segment to reveal a broad ~55 km × 50 km, ~1.5–2.0 km high, low height-to-width ratio, multipeaked, sediment-bare, shallow subducted oceanic relief. Owing to La Plata Island and the coastline being located, respectively, ~35 km and ~50–60 km from the trench, GPS measurements allow us to demonstrate that the subducted oceanic relief spatially correlates to a shallow, ~80 km × 55 km locked interplate asperity within a dominantly creeping subduction segment. The oceanic relief geometrical anomaly together with its highly jagged topography, the absence of a subduction channel, and a stiff erosive oceanic margin are found to be long-term geological characteristics associated with the shallow locking of the megathrust. Although the size and level of locking observed at the subducted relief scale could produce an  $M_w > 7+$  event, no large earthquakes are known to have happened for several centuries. On the contrary, frequent slow slip events have been recorded since 2010 within the locked patch, and regular seismic swarms have occurred in this area during the last 40 years. These transient processes, together with the rough subducted oceanic topography, suggest that interplate friction might actually be heterogeneous within the locked patch. Additionally, we find that the subducted relief undergoes internal shearing and produces a permanent flexural bulge of the margin, which uplifted La Plata Island.

**Plain Language Summary** Subducted seamounts play an important but still uncertain role in earthquake rupture processes, as seamounts are considered to subduct either aseismically or seismically. We use marine geophysical data across the central Ecuador convergent margin to reveal a broad ~55 km × 50 km, ~1.5–2.0 km high, shallow subducted oceanic relief of the Carnegie Ridge. New GPS measurements collected on La Plata Island and along the Ecuador coast allow us to demonstrate that the subducted oceanic relief spatially correlates to a shallow, ~80 km × 55 km locked interplate asperity within a dominantly creeping subduction segment. The oceanic relief geometrical anomaly together with its rough topography and the stiff oceanic Ecuador margin are found to be long-term geological characteristics associated with the shallow locking of the plate interface. Although the size and level of locking observed at the subducted relief scale could produce an  $M_w > 7+$  event, no large earthquake but frequent slow slip events and associated seismic swarms occurred within the locked patch. These transient processes together with the rough subducted oceanic topography support the view of a heterogeneous interplate frictional pattern within the locked patch. On a regional scale, the subduction of the oceanic relief has deformed the Ecuador margin and uplifted La Plata Island.

### 1. Introduction

The role of subducted seamounts on large earthquakes is still disputed [Watts *et al.*, 2010; Wang and Bilek, 2011; Bassett and Watts, 2015]. Some conceptual and mechanical models suggest that subducted seamounts locally increase the interseismic coupling (ISC) along the megathrust and act as seismic asperities or barriers to rupture during an earthquake [Cloos, 1992; Scholz and Small, 1997; Dominguez *et al.*, 1998; Yang *et al.*, 2012]. Conversely, seamount subduction has also been associated with weak interplate coupling [Kelleher

and McCann, 1976; Mochizuki et al., 2008; Singh et al., 2011; Marcaillou et al., 2016] and highly fractured media [Fisher et al., 1991; Dominguez et al., 1998; Wang and Bilek, 2011; Ruh et al., 2016], a situation that favors aseismic slip and relatively small earthquakes [Cummins et al., 2002; Mochizuki et al., 2008; Wang and Bilek, 2011]. Spatial associations between subducted seamounts and large subduction earthquakes have long been proposed [Kodaira et al., 2000; Husen et al., 2002; Bilek et al., 2003; Mochizuki et al., 2008; Sparkes et al., 2010; Singh et al., 2011; Duan, 2012; Hicks et al., 2012]. Since ISC is commonly used as a proxy for future earthquake, the availability of well-constrained ISC models now enables to further investigate this correlation. For instance, Kyriakopoulos and Newman [2016] showed that the area ruptured during the 2012  $M_w$  7.6 Nicoya earthquake was previously locked by a subducted elevated plateau localized 15–25 km beneath the Nicoya Peninsula. However, correlating the location of a subducted seamount with a shallow locked zone, such as in the Hikurangi margin [Bell et al., 2014], has remained a challenge because, where shallow subducted seamounts (<~15 km depth) are imaged [e.g., Park et al., 1999; Bangs et al., 2006; McIntosh et al., 2007; Barker et al., 2009], ISC is usually poorly resolved due to the lack of near-trench geodetic data [Geersen et al., 2015; Marcaillou et al., 2016; Wallace et al., 2009].

In central Ecuador, Vallée et al. [2013], Chlieh et al. [2014], and Nocquet et al. [2014] modeled the ISC using GPS data collected on La Plata Island (LPI) and at the Ecuadorian coastline, respectively, located ~35 km and ~50–70 km from the trench axis. Their models reveal a shallow (<15 km depth), ~80 km × 55 km locked asperity located below La Plata Island and extending to the trench. In this paper, we address the structural nature of that asperity and propose an updated ISC model. We use swath bathymetry, a combination of 2-D prestack depth migration of a grid of multichannel seismic reflection data, 2-D wide-angle seismic data collected offshore central Ecuador, and new GPS data to provide compelling evidence for a subducted oceanic relief locking the plate interface below and around La Plata Island. Each data set images the LPI locked region at different spatial and temporal scales, allowing to further discuss key factors that may control the tectonic behavior of the subducted oceanic relief and outer margin wedge, as well as potential interplate frictional anomalies within the locked patch.

## 2. Geodynamic Context, Seismicity, and Interseismic Coupling

The Ecuador margin, which belongs to the northeastward-escaping North Andean Sliver (Figure 1a) [Pennington, 1981; Yepes et al., 2016], is underthrust eastward at 4.7 cm/yr [Nocquet et al., 2014] by the young (<21 Ma) [Hardy, 1991] and morphologically complex Nazca Plate [Lonsdale and Klitgord, 1978]. The basement of the Ecuador margin consists of allochthonous Cretaceous oceanic terranes [Gansser, 1973; Gossens and Rose, 1973; Reynaud et al., 1999]. The terranes comprise the high- $V_p$  velocity (3.5–6 km/s) basaltic complex of the Piñon Formation that crops out on La Plata Island [Baldock, 1983] and extend close to the trench [Graindorge et al., 2004], where the margin outer wedge is erosive [Sage et al., 2006].

In central Ecuador, the offshore margin wedge is narrow and comprises a 20–50 km wide shelf and a 25–40 km wide outer wedge [Sage et al., 2006]. West of LPI (Figure 1b) multibeam bathymetry [Michaud et al., 2006] shows the outer wedge to consist of a smooth 6–7° trenchward-dipping slope that is gently scalloped downslope by a 50 km long and 10 km wide morphologic re-entrant (E1 in Figure 1b). Two small amplitude seafloor bulges (B1 and B2 in Figure 1b) protrude across the outer wedge slope, and the shelf edge adjacent to LPI reflects uplift with respect to its depressed northern and southern (E2 and E3 in Figure 1b) extremities, which echo local subsidence [Proust et al., 2016, Figure 3]. On the shelf, La Plata Island reaches 175 m in altitude and shows marine terraces cut in the basaltic basement. The island was uplifted at a 0.3–0.4 mm/yr rate during the Late Pleistocene (450–500 kyr) according to U-Th dating [Pedoja et al., 2006] and correlation with oxygen-isotope stages [Cantalamesa and Di Celma, 2004]. Offshore Ecuador, the Nazca Plate carries the east-west trending Carnegie Ridge (Figure 1a), a major 2 km high, 200 km wide seamount studded, volcanic ridge that results from the Neogene interaction between the Galapagos hot spot and the Cocos-Nazca spreading center [Lonsdale and Klitgord, 1978]. The subducting Carnegie Ridge is thicker (19 km from Sallares and Charvis [2003]) and more buoyant in its northern half compared to the 14 km thickness [Graindorge et al., 2004] of its southern half. Accordingly, subduction resistance forces may be higher in the northern Ecuador margin than in our study zone in central Ecuador. High-relief oceanic features carried along by plate motion likely influence the interplate coupling [Kelleher and McCann, 1976], deform the margin, and enhance subduction erosion [von Huene et al., 2004; Sage et al., 2006]. These features are more

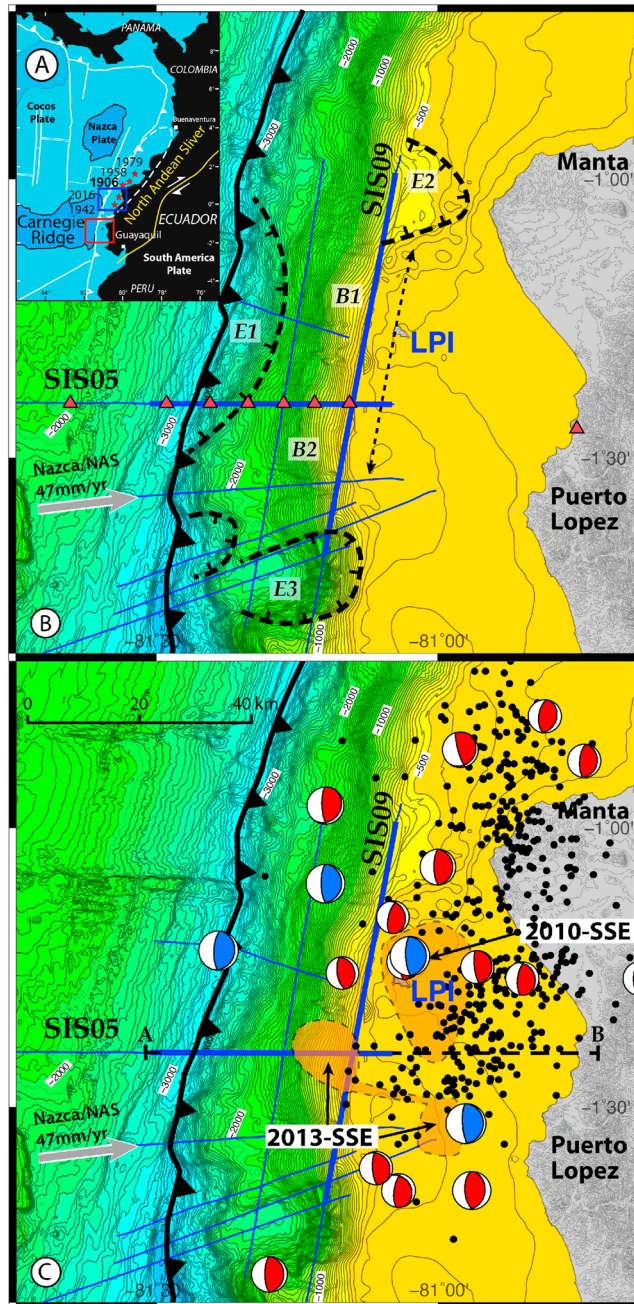


**Figure 1.** Bathymetry of the study area, location of seismic lines, background seismicity, focal mechanisms, and slow slip events. (a) Inset: the red frame is the location of the study area in central Ecuador where Carnegie Ridge is subducting; the red stars are 1906 to 2016 large to great subduction earthquakes; the blue frame is the location of Figure 10. (b) Multibeam bathymetric map of the study area [Michaud et al., 2006]; contour interval is 50 m; LPI is La Plata Island; the grey vector shows convergence between Nazca Plate and North Andean Sliver (NAS); the barbed line is the trench axis, and the ticked black dashed lines are morphologic re-entrants (E1, E2, and E3); B1 and B2 point to outer wedge seafloor bulges; the thin black dashed line with arrows shows N-S uplifted axis of La Plata Island (LPI) block; the blue lines are SISTEUR MCS reflection lines; the thick blue lines are MCS seismic lines SIS05 and SIS09 shown in Figures 2 and 3; the red triangles are ocean bottom and land seismometers along SIS04 wide-angle seismic line coincident with MCS line SIS05. (c) Background seismicity (black dots) from the RENSIG catalog (IG-EPN 1994–2007) relocated in an a priori 3-D velocity model [Font et al., 2013]; the red beach balls are 1976–2016 focal mechanisms from global CMT catalog (<http://www.globalcmt.org>); the blue ones were relocated in depth [Vaca et al., 2009]; the orange patches with black dash contours are 2010 [Chlieh et al., 2014] and 2013 [Segovia et al., 2015] slow slip events. Section A-B is the cross section presented in Figure 7.

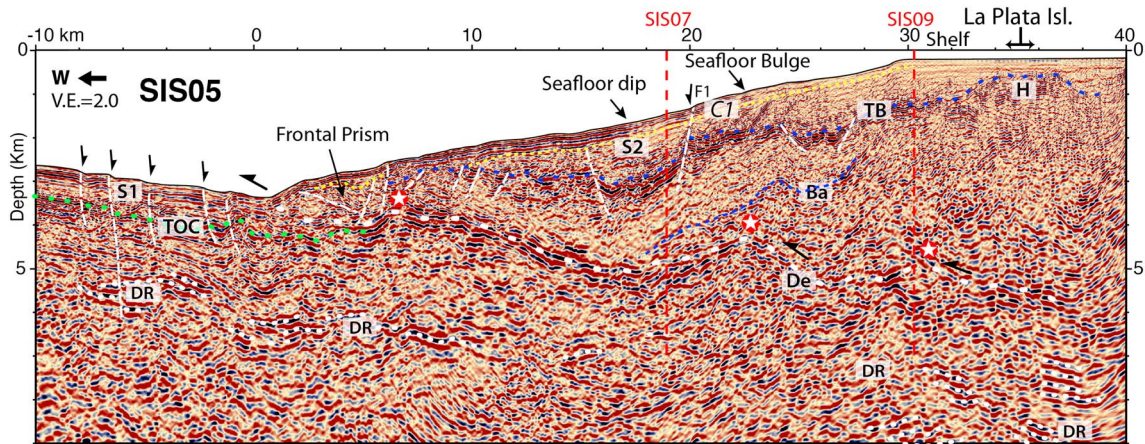


**Figure 2.** Prestack depth-migrated MCS line SIS05 located in Figure 1; S1 and S2 = sediment, C1 = late Pleistocene unconformity, TB = top of margin basement Ba, H = basement high adjacent to La Plata Island, De = interplate megathrust, white-red stars = main highs along De, DR = deep reflectors. Note that oceanic sediment S1 pinches out beneath the frontal prism, against the rough, low-angle trailing flank of the subducted oceanic relief supporting the local absence of a subduction channel further landward along the line.

numerous on the Carnegie Ridge southern flank. Their shapes range from low relief, 0.5 km high, 20–40 km wide tabular reliefs, to higher relief (1–2 km high), conical, and multiphase ~40 km long, steep-sided seamounts (Figure S5 in the supporting information). These features also include sediment bare and rough volcanic basement swells, such as the Carnegie Ridge eastern crest [Lonsdale, 1978].

Large and great megathrust earthquakes ( $7.7 < M_w < 8.8$ ) have repeatedly occurred in 1906, 1942, 1958, 1979, and 2016 along the northern Ecuador subduction interface (Figure 1a), north of Manta Peninsula [Kelleher, 1972; Kanamori and McNally, 1982; Beck and Ruff, 1984; Ye et al., 2016]. In contrast, only swarms of seismicity (Figure 1c) have occurred in central Ecuador, from northern Manta to Puerto Lopez [Holtkamp et al., 2011]. According to Font et al. [2013] the swarms concentrate beneath the shelf, in the overriding plate down to the plate interface. This seismicity was located in 3-D a priori *P* wave velocity model that integrates all available regional structural and velocity information. These 1 week to 3 month lasting  $M_w$  4.0 to 6.1 intense seismic swarms have been recorded in 1977 [Holtkamp et al., 2011], 1998, 2002, 2005 [Vaca et al., 2009; Font et al., 2013], 2010 [Vallée et al., 2013], and 2013 [Segovia et al., 2015]. The two latter were associated in time with a slow slip event (SSE) detected by GPS installed since 2009 (Figure 1c).

GPS data revealed that in the region of the 1942 and 2016 megathrust earthquakes, the updip segment of the plate interface is decoupled, whereas its downdip segment is characterized by a series of 15–30 km deep inter seismically coupled patches [Chlieh et al., 2014; Nocquet et al., 2014], two of them ruptured during the 2016  $M_w$  7.8 earthquake [Nocquet et al., 2016]. On the contrary, the plate interface in our central Ecuador study zone is governed by creeping with the exception of the shallow 50 km diameter, highly coupled LPI patch [Vallée et al., 2013]. At this location, the subduction interface modeled as a 12° landward-dipping planar fault appears to be locked from near the trench to ~12 km depth [Chlieh et al., 2014].

### 3. Crustal Structures Beneath the LPI Locked Patch

We used eight multichannel seismic reflection (MCS) lines and a wide-angle seismic (WAS) line (Figure 1b) collected offshore Ecuador onboard the IFREMER R/V *Nadir* during the 2000 SISTEUR cruise.

#### 3.1. MCS Processing and Prestack Depth Migration

MCS profiles were recorded using a 45 L air gun seismic source tuned in a single bubble mode and a 360-channel, 4.5 km long streamer. Shots were fired every 50 m, providing 45-fold coverage. All MCS lines were prestack depth-migrated (PSDM) [Al-Yahya, 1989; Thierry et al., 1999; Agudelo, 2005]. Accordingly, all lines were preprocessed using Geovecteur software to prepare for PSDM (see supporting information). To obtain accurate PSDM images along lines SIS05 (Figure 2) and SIS09 (Figure 3), a processing workflow based on a combination of velocities derived from MCS and coincident WAS data is applied [Agudelo et al., 2009] (see supporting information and Lines [1993] and Ross [1994]). Quality control and the accuracy of the

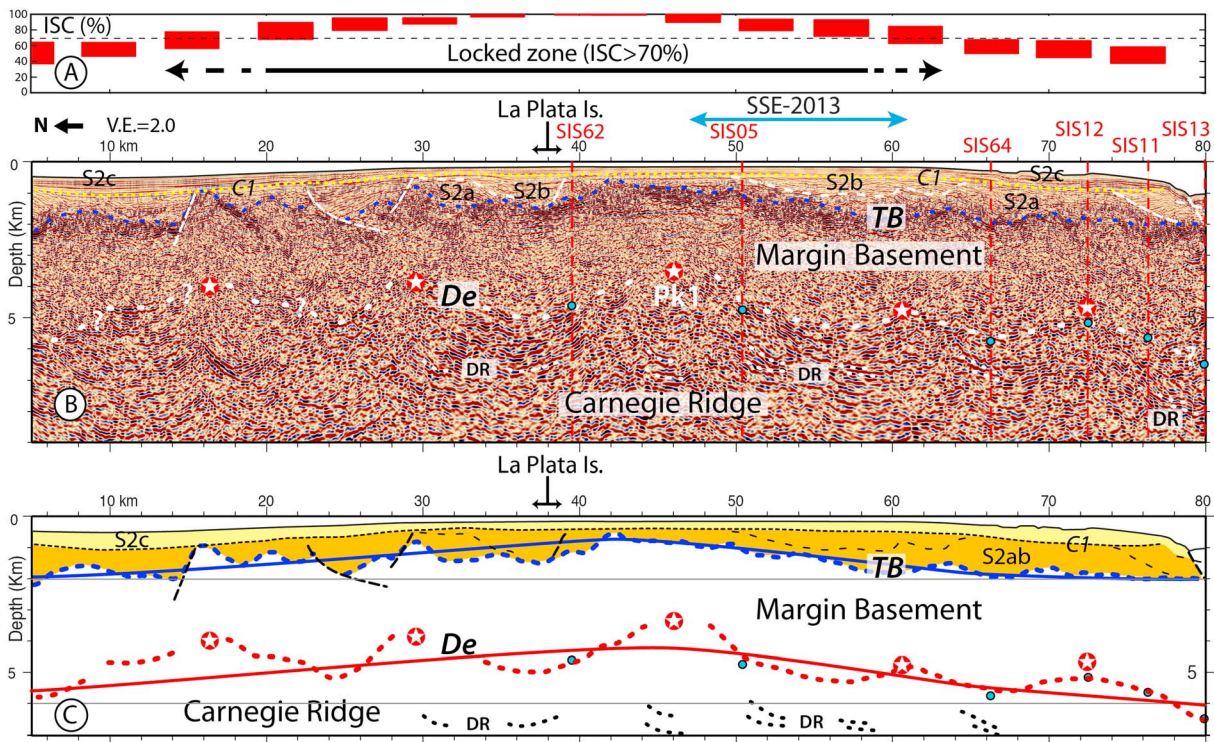


**Figure 3.** Prestack depth-migrated MCS line SIS09 with along strike ISC variations. The location is shown in Figure 1. (a) ISC variations with uncertainties (red bars) along the seismic line. (b) PSDM line SIS09; the blue dots along MCS line = location of the interplate megathrust from crossing PSDM MCS lines (vertical red-dashed lines), heavy white dashed-line De = interplate megathrust, TB = top of margin basement. Note the strong reflective character of the subducted Carnegie Ridge that contrasts with the poorly reflective bulk of the margin basement; S2ab = lower, mid-Cenozoic sediment, S2c = late Pleistocene system tracks [Proust *et al.*, 2016], C1 = late Pleistocene unconformity. The region of peaks (white-red stars) along the megathrust coincides with the highest ISC zone; the blue double arrow shows the 2013 SSE [Segovia *et al.*, 2015] likely extending between two peaks of the megathrust; DR = deep reflectors in the subducted Carnegie Ridge. C: continuous blue line is smooth margin basement top forming an ~1 km high bulge that mirrors continuous red line, which is smooth interplate megathrust.

migrated image are performed carefully by Common Image Gathers analysis (see supporting information) as they are a key point to our interpretation. At the crossing between lines SIS05 and SIS09, the estimated depth precision of the interplate fault at a 4.9 km depth is <300 m (see supporting information).

### 3.2. Wide-Angle Modeling of Line SIS04

WAS line SIS04 was collected along coincident line MCS SIS05 using 2 land stations and 10 ocean bottom seismometers (OBSs) with a 5 km spacing on the margin outer slope and a 128 L (128,048.52 cm<sup>3</sup>) air gun source fired every 125 m [Graindorge *et al.*, 2004; Gailler *et al.*, 2007] (Figure 1b). The SIS04 wide-angle velocity model of Graindorge *et al.* [2004] was revisited using forward modeling technique [Zelt and Smith, 1992] through a combination of first and secondary arrivals from OBS and land stations. Our new model (Figure 4) considers the geometry of major reflectors picked up from the PSDM coincident MCS line SIS05 (Figure 2), such as the margin basement top “TB,” the plate interface “De,” and the top of the oceanic crust “TOC.” These geometries were slightly adjusted to agree with WAS data when necessary. WAS record shows clear refracted and reflected arrivals from sedimentary and crustal layers. Identified phases and their names are indicated in Table 1. A shadow zone interpreted on OBS record sections 8 to 10 (OBS10 shown in Figure 5) between PB phase refracted in the margin basement, and P3a phase refracted in the lower plate oceanic layer 3a provides evidence for a velocity inversion beneath the margin wedge between upper plate layer B or C and lower plate oceanic layer 2.

### 3.3. Results

Among the MCS lines collected near LPI across the outer margin wedge, we show EW-trending MCS line SIS05 and NS-trending MCS line SIS09, which are most representative of the 3-D structural characteristics of the plate interface.

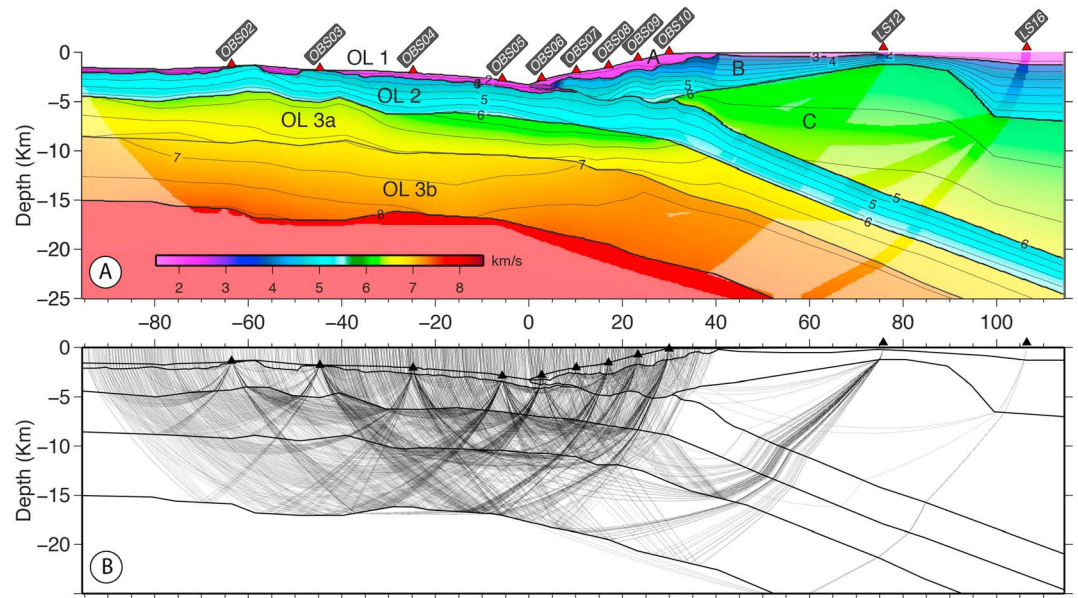


**Figure 4.** Results from forward modeling for wide-angle seismic line SIS04. (a) Final *P* wave velocity model obtained from joint modeling of wide-angle seismic data and coincident multichannel seismic reflection line SIS05; areas constrained by ray-tracing are shaded; OBS = ocean bottom seismometer, LS = land station. Downgoing plate: OL1, OL2, and OL3a and b = oceanic layers 1, 2, 3a, and 3b, respectively. Margin: A = shallow sediments of layer A, B = upper crustal layer B, C = lower crustal layer C. (b) Ray coverage for all diving and reflected waves with every five ray from two-point ray tracing model.

**3.3.1. A Shallow Dipping and Highly Uneven Plate Interface**

Seismic line SIS05 (Figures 2 and S1) cuts across the outer margin wedge and outer shelf, 15 km south of LPI (Figure 1). Well-stratified Carnegie Ridge sediment layer S1 and high-amplitude, top of oceanic crust TOC reflector extend landward beneath the margin, although layer S1 sharply terminates beneath a 5 km wide frontal prism. In contrast, TOC reflector, whose amplitude is locally enhanced, extends farther downdip in the form of the De reflector, to an ~6 km depth beneath the shelf. About 3 km beneath De reflector, the subducted Carnegie Ridge returns energetic and discontinuous reflections DR indicating strong internal impedance contrast.

De reflector dips ~3° on average beneath the margin wedge and is characterized by three remarkable 0.5 to ~1 km high, 5–8 km wide knolls and peaks. Layer S1 that pinches out beneath the frontal thrust, at the toe of the shallowest peak, supports the absence of a subduction channel further downdip along the line. Thus, the

**Table 1.** Observed Seismic Phases, Residual Travel Times, and  $\chi^2$  Errors for the Wide-Angle Forward Velocity Model of Line SIS04

Layer	Observed Phases	Phase Name	Number of Picks	RMS Misfit (s)	$\chi^2$ Error	Uncertainty
Layer A	Refracted wave within layer A	PA	132	0.079	1.047	0.060
Layer A	Reflection from the base of layer A	PrA	191	0.041	0.076	0.150
Layer B	Refracted wave within layer B	PB	559	0.081	2.607	0.050
Layer B	Reflection from the base of layer B	PrB	288	0.057	0.516	0.080
Layer C	Refracted wave within layer C	PC	35	0.040	1.047	0.040
Layer 1	Refracted wave within oceanic sediments layer 1	P1	49	0.073	0.245	0.150
Layer 1	Reflection from the base of oceanic sediments layer 1	Pr1	143	0.047	0.275	0.090
Layer 2	Refracted wave within oceanic layer 2	P2	864	0.072	3.246	0.040
Layer 2	Reflection from the base of oceanic layer 2	Pr2	858	0.052	0.269	0.100
Layer 3a	Refracted wave within oceanic layer 3a	P3a	2365	0.121	5.841	0.050
Layer 3a	Reflection from the base of oceanic layer 3a	Pr3a	1075	0.073	0.665	0.090
Layer 3b	Refracted wave within oceanic layer 3b	P3b	1322	0.070	0.497	0.100
Layer 3b	Reflection from oceanic Moho	PmP	1540	0.089	0.352	0.150
Mantle	Refracted wave from upper mantle	Pn	85	0.129	0.753	0.150
Total			9506	0.088	2.183	

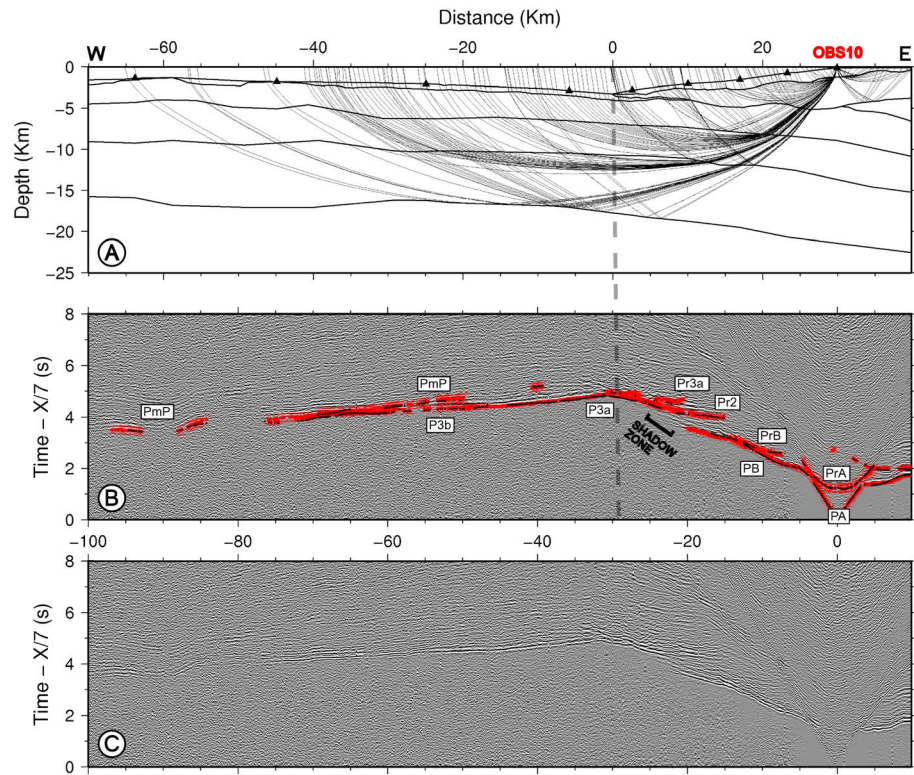


**Figure 5.** Wide-angle seismic record section of OBS10 located above the subducted oceanic relief. (a) Ray tracing in the forward model for OBS10. (b) Record section with picks arrivals (red circles with error bars) and calculated travel times through the model (dark circles); labels correspond to the picked phases (see Table 1 and Figure 4). (c) Uninterpreted OBS10 seismic record.

strong and highly uneven De reflector, which extends from the trench axis downdip and truncates the margin basement reflectors, is interpreted as the plate interface megathrust. The shallow-dipping plate interface is hence inferred to warp across a broad, sediment-bare, multiphase subducted basement relief.

Along line SIS05, the strong top of the basement reflector TB is disrupted and overlain by well-stratified, 0.5–1.5 km thick layer S2. As the subducted peaks come into contact with the base of the margin basement, a paired seafloor bulge and dip (Figure 2) reveals that the outer wedge gently deforms, conforming to the plate boundary topography. Indeed, both the basement and TB reflector are deformed by high-angle normal faults, defining small horst and grabens (at 18 and 26 km). Normal fault F1 appears to cut through layer S2 and deforms the seafloor, indicating that the area is undergoing extension.

Seismic line SIS09 (Figures 3 and S2) cuts across line SIS05 on the shelf edge and passes only ~5 km seaward of LPI. Plate interface “De” is pinpointed from (1) its location on the six dip MCS lines that crosscut line SIS09 and (2) the boundary between the strongly reflective character of the subducted Carnegie Ridge and the overlying poorly reflective bulk of the margin basement. The reflective contrast is best defined at 33–44 km and 50–60 km along the line. From 33 to 80 km along the line, plate interface “De” proves highly uneven, showing three ~0.5–1.5 km high subducted peaks, the shallowest (Pk1 in Figure 3) culminating at an ~3.5 km depth, although the image of its summit remains unclear. The interpretation of the plate interface north of 33 km along the line is tentative as dip line control is lacking and the plate interface is weakly reflective. The plate interface seems, however, to deepen northward, and two more peaks at 30 and 16 km are considered based on the shape and depth of discrete reflectors. On a large scale, uneven plate interface De can be fitted by a smooth curve with 2–4° slopes. The curve outlines a broad ~1.5–2.0 km high, subducted basement bulge centered on Pk 1 (Figure 3c). The curve that smoothes out margin basement reflector TB forms as well, a broad ~1 km high margin basement bulge that mirrors the smooth curve associated with underlying plate interface De, suggesting a cause-and-effect relationship between them. The bulge of basement reflector TB is shallowest (~0.5 km) at 42 km close to LPI. The reflector deepens to 2 km

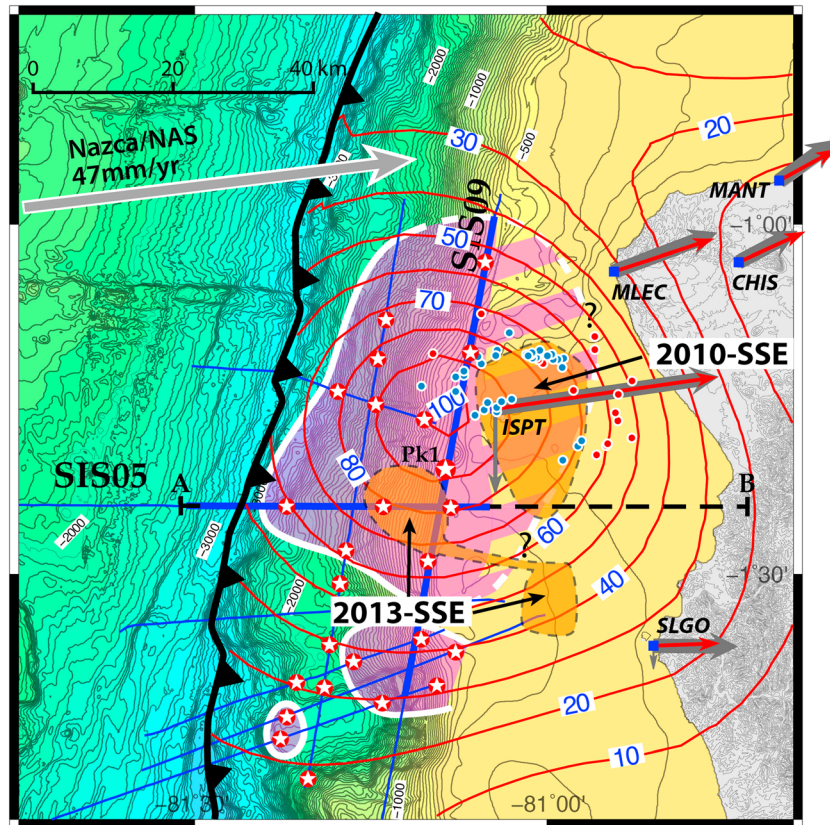


**Figure 6.** Interpreted geographic extension of the subducted oceanic relief and interplate lock patch modeled from GPS data. The transparent pink body with thick white contour is estimated extent of the broad subducted oceanic relief with peaks (red/white stars along MCS lines). The striped yellow/pink area bordered by white dashed line is presumed leading flank of the subducted oceanic relief. The dark grey arrows are observed GPS horizontal velocities expressed with respect to the North Andean Sliver; the italic letterings are GPS station names as in Table 2; the red arrows are modeled GPS horizontal velocities corresponding to the optimal spatial distribution of interseismic coupling ( $0 < ISC < 100\%$ ) taking into account the plate interface geometry with the subducted oceanic relief (see Figure S5); the thin downward grey arrows are observed vertical GPS velocities (see Table 2); the red contours are modeled ISC each 10%. Note that the highly coupled zone ( $ISC > 70\%$ ) coincides spatially with the location of the subducted oceanic relief and that the 2010 and 2013 slow slip events (orange patches with black dash contours) occurred in the locked patch. The microseismicity associated with the 2010 SSE [Vallée et al., 2013] (blue dots = depth < 10 km; red dots = depth > 10 km) is shown.

northward of 40 km, where it is disrupted by inactive faults associated with buried basement highs. Southward of 40 km, TB reaches an ~2 km depth at 75 km and is generally flatter and less disrupted than north of 40 km. The basement sedimentary cover, which is thinnest along the shelf edge between 30 and 55 km, thickens to ~1.5 km over both flanks of the bulge. S2a/S2b lower and mid-Cenozoic sediment has accumulated in small slope and shelf basins controlled by the faults across the bulge northern flank. The faults were sealed by unconformity C1 dated >800 kyr [Proust et al., 2016], which eroded most of S2a/S2b sediment between 30 and 55 km along the line. Unconformity C1 is overlain by late Pleistocene transgressive-regressive system tracks of sedimentary layer S2c [Proust et al., 2016].

From reflector De interpreted on all MCS lines in Figure 1, we constructed a simplified 3-D geometry of the plate interface. It outlines a collection of closely spaced knolls and peaks that belong jointly to the broad, ~55 km long, at least 40 km wide, low (4%) height-to-width ratio, subducted Carnegie Ridge basement relief (Figure 6).

### 3.3.2. A $V_p$ Velocity Model of the Subducted Oceanic Relief and Margin Wedge

Modeling the shadow zone observed on OBS record sections 8 to 10 (Figure 5) provides evidence that 4.8–5.0 km/s  $V_p$  rocks of the top section of the subducted oceanic relief wedge beneath higher velocity rocks (5.8–6.0 km/s) of the deepest section of the margin oceanic basement (Figure 7a). Such a low-velocity zone marks the top of the subducted oceanic relief. The quality of the forward model can be evaluated by

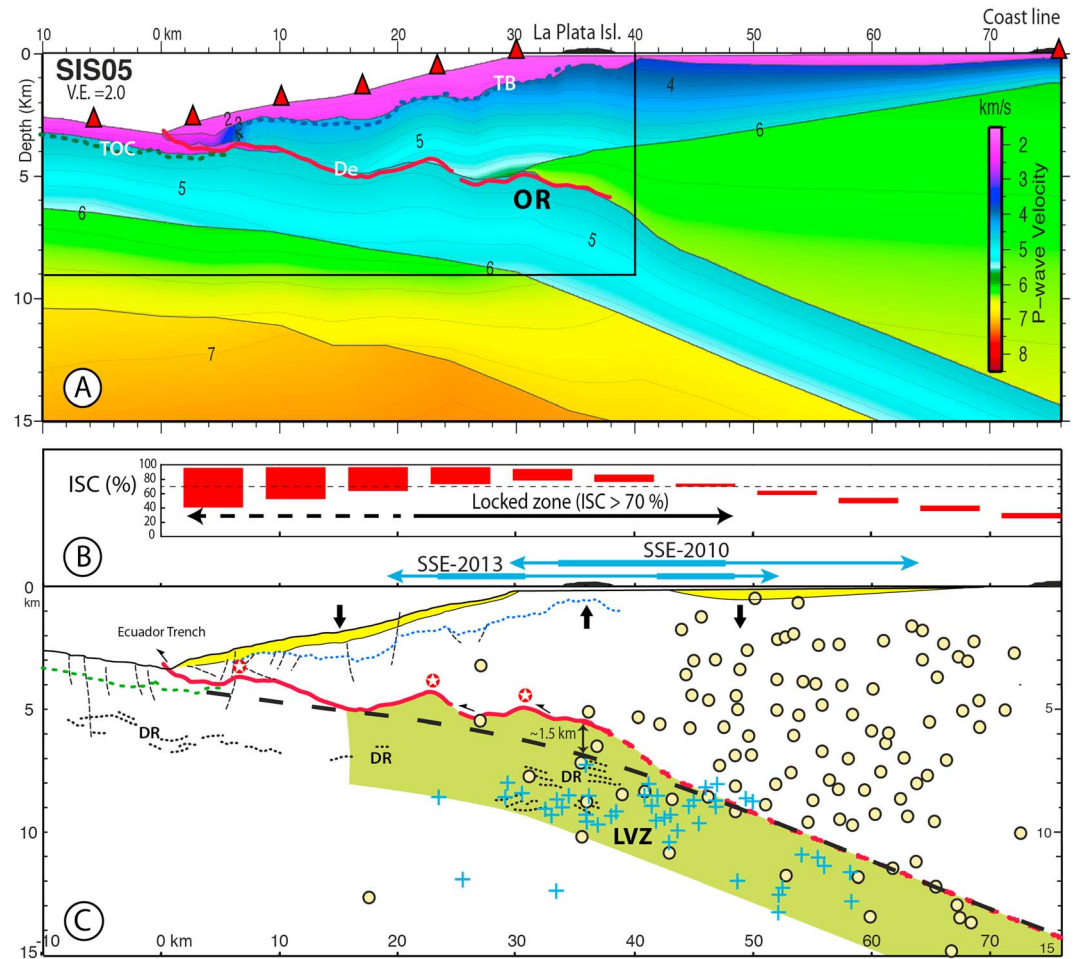


**Figure 7.** Spatial correlation between the subducted oceanic relief and the megathrust locked zone along cross-section AB located in Figure 6. (a) Section showing the superposition of De interplate megathrust (red curve in the frame from MCS line SIS05) onto the wide-angle seismic velocity model of OBS line SIS04; LPI is projected onto the section; the red triangles are ocean bottom and land seismometers; OR is subducted oceanic relief. TB, TOC, and De as in Figure 2. (b) ISC down dip variations (%) with uncertainties (red bars) along cross-section AB. Note that the area of ISC >90% lay further north of this section (Figure 6); the blue double arrows show the extent of the 2010 and 2013 slow slip event (SSE) after *Chlieh et al.* [2014] and *Segovia et al.* [2015]. (c) Margin structures and seismicity; the yellow layer shows late Pleistocene sediment [*Proust et al.*, 2016]; the vertical black arrows indicate vertical motions of margin basement in response to the oceanic relief subduction; stars as in Figure 2; the heavy black dashed line shows the regional subduction interface based on *Hayes et al.* [2012]; note the spatial correlation between the rough subducted oceanic relief and the megathrust locked zone (ISC > 70%); LVZ (green) = downgoing plate low velocity zone; relocated 1994–2007 seismicity within the inner margin wedge (yellow dots from *Font et al.* [2013]) and microseismicity triggered by the 2010 SSE event (blue crosses [*Vallée et al.*, 2013]) laying dominantly within the subducted oceanic relief and LVZ.

estimating the difference existing between picked and predicted travel times. The final velocity model was obtained for a satisfying RMS (root-mean-square) error of 0.088 s using 9524 picks (95% of the total picks). Further details on quality parameters such as RMS error,  $\chi^2$ , and number of data used for all phases are given in Table 1.

Ray tracing between source and receiver across the model allows discriminating between well-resolved and poorly or unconstrained areas. Sedimentary and crustal layers are crossed by both diving and reflected arrivals. Ray coverage is of good quality particularly between –50 and 30 km distance along the model (Figure 4b). The plate interface “De,” i.e., the top of the oceanic relief extracted from MCS data, was sampled using the PrB reflected phase from the OBS06 to the OBS10 (Figure 5b), although the PrB phases are relatively weak due to the rough topography and the velocity inversion at the top of the oceanic relief. Geometrical details from the MCS major reflectors were preserved as long as they improved the overall velocity model fit. The absence

**Table 2.** GPS Results

Longitude	Latitude	V <sub>east</sub>	V <sub>north</sub>	S_V <sub>north</sub>	S_V <sub>east</sub>	Code
-80.12845	-0.71117	5.460	-1.517	0.532	0.532	OLIM
-80.53623	-0.91666	4.837	4.140	0.823	0.823	BRBR
-80.22297	-1.84095	2.237	0.954	0.713	0.713	SABA
-80.38716	-1.18271	3.205	2.094	0.620	0.419	STAA
-79.50906	-1.18711	-0.770	-2.455	0.630	0.630	MOCA
-79.53069	-1.55888	0.515	-0.526	0.218	0.218	PUEB
-79.90861	-1.36748	1.843	0.688	0.319	0.728	BALZ
-80.38716	-1.18271	3.205	2.094	0.620	0.419	STAA
-80.67116	-0.93660	6.646	4.803	0.420	0.622	MANT
-79.99554	-1.87655	-0.708	0.682	0.180	0.230	DAUL
-79.55386	-1.89429	1.774	-0.867	0.791	0.791	JUJA
-80.75686	-1.98853	-0.047	-0.733	0.367	0.367	AYAN
-80.90515	-2.21914	1.737	1.448	0.201	0.221	LIBF
-81.07355	-1.26214	26.347	3.797	0.182	0.151	ISPT <sup>a</sup>
-80.42520	-1.55240	3.147	-0.038	1.938	1.570	PJEC <sup>a</sup>
-80.84913	-1.60001	9.942	-0.100	0.906	0.813	SLGO <sup>a</sup>
-80.39786	-0.65892	7.511	0.323	0.416	0.328	BAHI <sup>a</sup>
-80.01166	-1.54827	2.197	0.174	0.909	0.869	COLI <sup>a</sup>
-80.03402	-0.97382	3.884	0.004	0.626	0.572	SEVG <sup>a</sup>
-80.72840	-1.05307	6.904	3.655	0.455	0.378	CHIS <sup>a</sup>
-80.47456	-1.05804	2.618	1.539	0.759	0.688	PTEC <sup>a</sup>
-80.90563	-1.06638	12.180	4.581	0.440	0.530	MLEC <sup>a</sup>
-80.42870	-0.38647	12.840	6.861	0.332	0.301	CABP <sup>a</sup>
Longitude	Latitude	V <sub>Up</sub>	S_V <sub>up</sub>	Code		
-80.72840	-1.05307	0.653	1.932	CHIS		
-81.07355	-1.26214	-5.222	1.867	ISPT		
-80.84913	-1.60001	-2.756	2.156	SLGO		

<sup>a</sup>Continuous GPS stations. Top: longitude and latitude of GPS sites in decimal degrees. V<sub>east</sub> and V<sub>north</sub> are interseismic velocities with respect to the North Andean Sliver, and S\_V<sub>north</sub> and S\_V<sub>east</sub> are the associated uncertainties (1 $\sigma$  confidence level) in mm/yr. Bottom: same as above for the vertical velocities used in the study. Vertical velocities are with respect to the ITRF2008.

of reverse shots both on land and across the shelf results in lower ray coverage east of the OBS10, where only arrivals from two land stations were included in the model. Hence, because the dip angle of the leading flank of the oceanic relief is unconstrained from MCS data and poorly resolved from OBS data, we used the Slab 1.0 model of the regional subduction isodepths [Hayes *et al.*, 2012] and the local distribution of seismic events [Font *et al.*, 2013] to constrain the dip of the subduction interface from La Plata Island to the coastline. This 11° dip and the ~15 km depth beneath the coastline allowed constructing a conservative and geologically realistic model of the subducted uneven basement relief (Figure 7).

## 4. A Refined ISC Model in the LPI Region

### 4.1. GPS Data Set

To better constrain the ISC spatial distribution in the area of La Plata Island, we used a denser network of GPS data than that used by Vallée *et al.* [2013] and Chlieh *et al.* [2014]. The data set includes 23 GPS sites analyzed together with the data presented in Nocquet *et al.* [2014] and 30 continuous GPS (CGPS) sites surrounding Ecuador from the global network of the International Global Navigation Satellite Systems Service for Geodynamics (<http://igsceb.jpl.nasa.gov>). Our solution includes new CGPS sites operated by the Instituto Geofísico de la Escuela Politécnica Nacional [Mothes *et al.*, 2013] (BAHI, MLEC, SLGO, and COLI) and the Instituto Geográfico Militar (PTEC) and two campaign sites (JUJA and STAA). Figure S5 shows the location of the GPS sites in the LPI area, and all interseismic velocities are provided in Table 2. Each GPS campaign site selected in the present study benefits from at least three campaigns spanning at least 4 years. All CGPSs have a minimum of 2.5 years of measurements to mitigate the impact of seasonal variations on the velocity estimates [Blewitt and Lavallée, 2002].

Large velocity differences were found between campaign sites averaging the velocity over the 1994–2011 period used in *Nocquet et al.* [2014] and *Chlieh et al.* [2014]. This difference is possibly due to frequent SSEs occurring in this area. Here for campaign sites, we only kept the period corresponding to the time period when the CGPS network was operating so that we could ensure that no SSE biases the velocity estimates.

#### 4.2. GPS Data Analysis

Campaign and continuous data have been analyzed simultaneously for the 2008.0–2016.0 period, with the GAMIT/GLOBK software [*Herring et al.*, 2010], using a standard strategy for geodynamics. We used the cumulative up-to-date solution from the International Global Navigation Satellite Systems Service (<http://igsceb.jpl.nasa.gov>) as our reference to express our velocity field with respect to the ITRF2008 [*Altamimi et al.*, 2011], using a 14-parameter transformation. All velocity uncertainties account for time-correlated noise in the GPS time series. More specifically, noise parameters (level of white noise, fractional integer noise index, and level of fractional integer noise) were first estimated from the time series for continuous sites, using the maximum likelihood estimator implemented in the CATS software [*Williams*, 2008]. We used the Euler pole derived by *Nocquet et al.* [2014] for the North Andean Sliver to obtain the final velocity in the frame of the overriding plate, which is eventually used as input data for the modeling.

Aside from the horizontal velocities, we also used the vertical velocity at ISPT, CHIS, and SLGO because (1) the quality and the length of their time series (between 4 and 7 years) enabled to estimate the velocity with the 1 mm/yr precision and (2) they are the closest sites from the area of interest in this study, providing additional constraints in the ISC inversion. Because vertical velocities are more sensitive to the elastic structure than horizontal ones and because the ITRF2008 reference frame might not be adequate to represent the zero of the overriding plate (as implicitly assumed by the elastic model), we added a 1 mm/yr uncertainty to vertical velocity standard deviation in the inversion (see supporting information for the details of GPS analysis).

#### 4.3. Inversion of Interseismic Coupling

We use the virtual back slip approach described in *Savage* [1983] to model the interseismic spatial coupling (ISC). The rake and the convergence velocity are fixed to be consistent with the Nazca Plate/North Andean Sliver motion as defined in *Nocquet et al.* [2014]. The subduction interface from latitude 0.25° to 2.0°S is discretized into 1214 quasi-equilateral triangular subfaults with an average edge length of 4 km (Figure S5). Our triangular mesh follows the SLAB1.0 geometry [*Hayes et al.*, 2012] for the South America subduction interface, except in La Plata Island area, where the oceanic relief geometry is included (Figure S5) and is modeled by a Gaussian function of 2 km height, half-width of 25 km in latitude and 10 km half-width in longitude, providing a good fit to the grid of MCS profiles used in this study (RMS = 1 km). The extent of the grid used in the inversion is much wider than the area of interest to avoid bias in our results that may arise when not considering contribution of segments adjacent to neighboring segments to the velocity field. Our inversion strategy follows the linear Bayesian approach proposed by *Tarantola* [2005] where the regularization is imposed through a covariance matrix controlling the level of smoothing of the solution and damping with respect to an a priori model. Classical resolution analysis for linear least squares inversion indicates that coupling as close as ~15 km from the trench can be retrieved in front of LPI. Along strike, a good resolution (restitution index > 0.5) is found from the coast to ~30 km and ~40 km landward from the trench, north, and south of LPI, respectively (Figure S6). We further investigate the range of possible models by exploring a wide range of regularization parameters (Figure 8). All details about the inversion method and resolution analysis are provided in the supporting information [*Okada*, 1992; *Hansen and O'Leary*, 1993; *Stark and Parker*, 1995; *Loveless and Meade*, 2011; *Radiguet et al.*, 2012].

As a summary of our tests, we find that (1) there is a highly locked patch (ISC > 70%) roughly centered around LPI (Figure 6); (2) the along strike variation of coupling is well constrained from the coast to the longitude of LPI, showing a decrease of coupling northward and southward of LPI. ISC < 50% is found ~25 km south and north of LPI; (3) high coupling is further resolved up to ~20 km west of LPI; and (4) there is low constrain on ISC very close to the trench at the latitude of LPI, and from the trench to ~25 km and ~35 km landward, north and south of LPI, respectively, leaving high or low coupling equally possible. Although (4) prevents any correlation to be demonstrated between high ISC and the subducted oceanic relief, (1)–(3) show that the high ISC area spatially correlates with the location of the oceanic relief where geodetic data are well resolved.

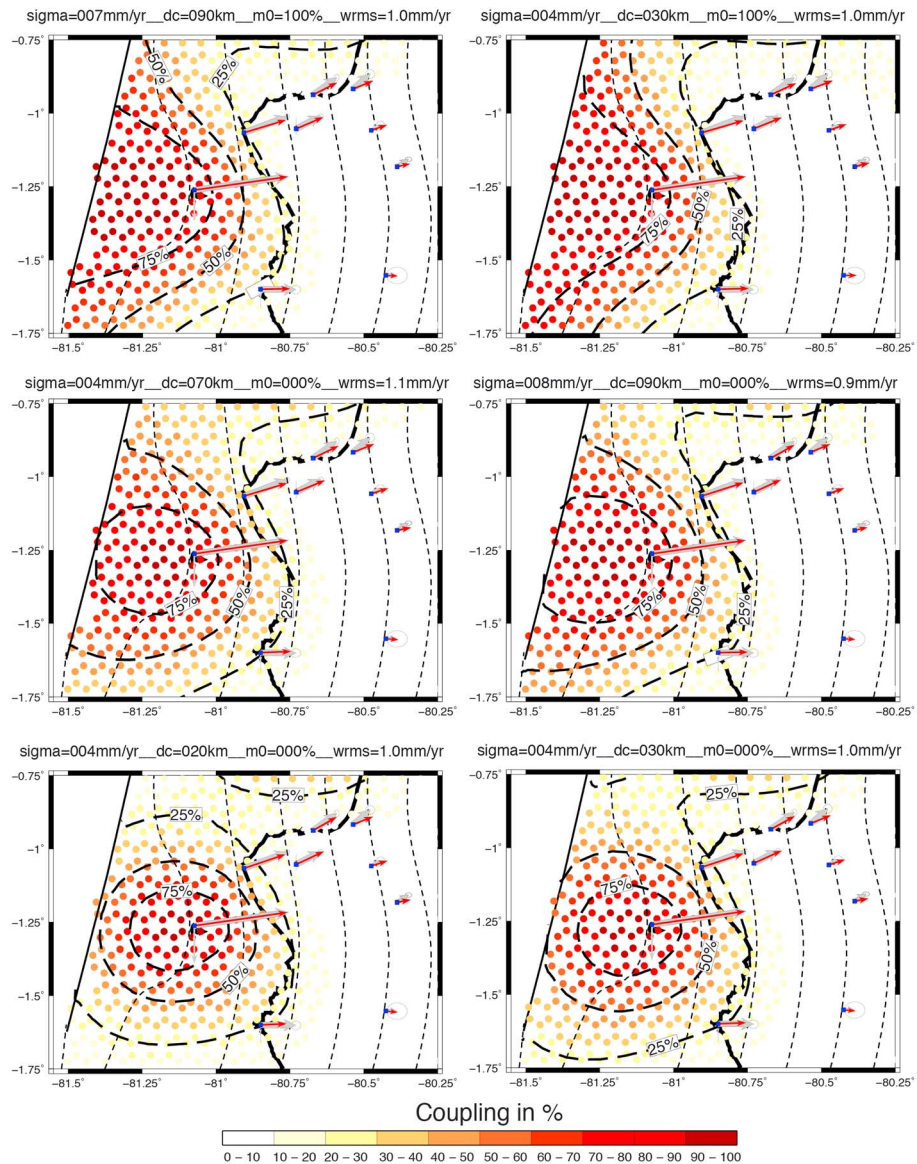


**Figure 8.** Selection of ISC models passing the  $\chi^2$  test and the  $L$ -curve criterion (Figure S7). The models are ordered from (bottom left) minimum to (top right) maximum coupling. The bottom-right model is shown in Figure 6. The bold dash lines indicate isovalues of coupling for 25%, 50%, and 75%, respectively. The grey and red arrows are GPS data and results of the model; the short dash lines are isodepth contours for the subduction interface every 5 km; the simplified oceanic relief geometry is included in the 5 km isodepth contour.

The ISC pattern, vanishing downdip and laterally around the proposed oceanic relief location, provides a strong evidence of the causal relationship for high coupling in this area. The resolution is high between LPI and the coastline where high ISC argues for a highly locked leading flank of the subducted oceanic relief. Good resolution found up to  $\sim 20$  km westward of LPI supports the view that the trailing flank of the oceanic relief is also highly locked, at least at this latitude.

## 5. Discussion

### 5.1. Margin Deformation Induced by the Subducted Oceanic Relief

Both the MCS images and the WAS velocity model show coherent evidences for the broad ( $\sim 55$  km  $\times$   $> 40$  km), low height-to-width ratio subducted Carnegie Ridge basement rise that has a maximum  $\sim 1.5$ – $2.0$  km height above the otherwise smoothly curved Slab1.0 [Hayes *et al.*, 2012] plate interface model.

Overall, the seamount geometrical resistance to subduction likely concentrates significant stress in the adjacent surrounding medium, hence resulting in long-term margin deformation, such as a lower slope morphologic reentrant and a topographic bulge that propagates through the margin wedge followed by subsidence after the subducting relief has passed [Collot and Fisher, 1989; Fisher et al., 1991; Dominguez et al., 1998; Dominguez et al., 2000; Taylor et al., 2005; Wang and Bilek, 2014; Bassett and Watts, 2015; Ruh et al., 2016]. Noticeable structural evidences support this assertion in the LPI region: (1) the subtle morphologic scar left by the oceanic relief at the toe of the margin slope, together with (2) the gentle bossing effects (Figure 1b) on the upper margin slope associated with the subducted peaks; (3) normal faults that crosscut the margin outer wedge, above the subducted relief; (4) the broad, ~55 km long, ~1 km high outer shelf margin basement bulge that correlates with the ~1.5–2.0 km high, subducted basement bulge (Figure 3c); and (5) the recent uplift of LPI attested by late Pleistocene marine terraces [Cantalamesa and Di Celma, 2004; Pedoja et al., 2006]. Additionally, the sequential stratigraphic analysis of late Pleistocene sediment (layer S2c in Figure 3) imaged by high-resolution (HR) seismic data reveals substantial vertical deformation of the shelf and upper margin slope in the LPI region. The analysis advocates that subsidence of the shelf edge in front of Manta and LPI and in a shelf piggyback basin forming southeastward of LPI occurred at least since ~790 kyr, while the seafloor in the LPI region started uplifting prior to ~533 kyr [Proust et al., 2016]. Uplift evidenced by an ~533 kyr angular unconformity carried on in the LPI region, while the piggyback basin was deformed and tilted, its depot center migrating eastward [Proust et al., 2016]. At ~337 kyr, upward bulging of the acoustic basement affected the shelf edge and interrupted sedimentation in the immediate periphery of LPI, while sedimentation persisted in the piggyback basin [Martillo et al., 2013]. Other HR seismic data suggest ~240 m of post ~130 kyr uplift of the northern bound of the LPI region. Hence, late Pleistocene downwarping reaches ~400 m in the piggyback basin and ~750 m beneath the shelf edge offshore Manta and LPI, while uplift in the LPI region achieves several hundred meters (Figure 7). In map view, the piggyback basin surrounds the eastern flank of the LPI-centered, basement bulge [Proust et al., 2016, Figure 12] reflecting a specific, long-term, nonelastic 3-D flexural bulge of the margin basement. We believe that this flexural bulge is controlled by the subduction of the oceanic relief because (1) the oceanic relief underlies the entire outer margin wedge and outer shelf and locks the megathrust and (2) its subduction time frame coincides with the timing of the specific shelf deformation pattern. Indeed, based on a 4.7 cm/yr convergence rate [Nocquet et al., 2014], peak PK1 that presently underlies the shelf edge (Figure 6) clogged the trench some 750 kyr ago. This timing also supports that the leading flank of the oceanic relief impinged earlier upon the margin toe.

The relatively subdued scar left in the margin wedge by the subducted oceanic relief may appear surprising. As shown by analog and numerical models [Lallemand and Le Pichon, 1987; Dominguez et al., 1998; Ruh et al., 2016], the structural imprint of subducted seamount depends on parameters including the seamount shape and its height-to-width ratio, as well as the relative margin and seamount rock strength, strain weakening, and the plate interface strength. As indicated by many natural examples [Fisher et al., 1991; von Huene et al., 2000], seamounts higher than 3 km with steep flanks ( $>5^\circ$ ) tend to fracture more severely the margin with strike-slip faults and back thrusts and leave a more profound indent in the inner trench slope than low relief seamounts [Dominguez et al., 1998]. However, in the Mariana Trench, subduction of large seamounts has not produced significant deformation in the fore arc, an observation that is potentially related to the ductile behavior of margin mantle rocks and/or to progressive fracturing of the subducting plate [Oakley et al., 2008]. As a seamount underthrusts the deep cohesive part of the margin, its topographic seafloor expression and structural imprint reveal less pronounced [Ruh et al., 2016]. It shows only gentle seafloor uplift, without a detectable fracture network, but normal faults are inferred in the wake of the seamount [Dominguez et al., 1998]. In the LPI region, the low height-to-width ratio of the subducted oceanic relief and potential plastic deformation of the fore-arc crust around the subducted relief may account for the relatively low amount of surface uplift above the subducted topography and modest extensional faulting in the margin outer wedge, although the strong ISC related to the oceanic relief geometrical anomaly likely explains the shelf basement flexural bulge.

## 5.2. Potential Interplate Frictional Anomalies Within the LPI Locked Patch

Although high ISC confined along a narrow strip close to the trench cannot be ruled out, our main result demonstrates that the subducted oceanic relief locally increases the ISC (Figure 6), in an otherwise dominantly creeping interface segment, a finding that confirms the model proposed by Scholz and Small [1997],

although the ISC mechanism might differ from their proposal. Yet as shown by the resolution tests (Figure S6) both the oceanic relief leading and trailing flanks are strongly coupled ( $ISC > 70\%$ ) as far downdip as  $\sim 9\text{--}10$  km (Figure 7). The results presented herein are derived from an erosive oceanic margin, the high  $V_p$  igneous basement of which extends close to the trench. They are, however, consistent with the high coupling value considered by *Bell et al.* [2014] at the leading flank of a seamount subducted beneath the Hikurangi accretionary wedge. However, the high ISC level found across the Ecuador subducted relief trailing flank contrasts with the very weak coupling assumed by *Bell et al.* [2014] on the seaward flank of the Hikurangi seamount.

As proposed by *Wang and Bilek* [2014] in a generic model, we interpret the locking of the LPI patch at the oceanic relief scale to be caused by a large resistance to fault motion due to the geometrical anomaly of the basement relief and its peaks with respect to a planar fault, rather than to a strong frictional contact over the whole patch. In absence of a denser GPS network or absolute pressure gauge measurements offshore, it might be that the locking observed below LPI is more heterogeneous than obtained from our ISC inversion. The apparently homogeneous ISC might come from the effect of the elastic medium that filters small-scale heterogeneity of slip rates at the plate interface. Additionally, some weak patches might appear locked because they lie in the stress shadow of actually locked smaller scale patches [*Wang and Dixon*, 2004; *Perfettini et al.*, 2010]. Three lines of evidence advocate for the area of high ISC around LPI to be actually more heterogeneous than determined from geodetic data.

1. Repeated shallow earthquake swarms, the largest events of which ( $4.9 < M_w < 6.1$ ) exhibit thrust motion (<http://www.globalcmt.org>), occur frequently within the LPI locked patch (Figure 1c). Four  $M_w$  5.9–6.1 thrust events of the 2005 swarm (Figure 1c) were relocated and modeled by waveforms inversion to provide improved  $\sim 7$  to 12 km focal depths [*Vaca et al.*, 2009], indicating that they ruptured isolated asperities of the plate interface in the locked patch. Their thrust plane dips  $18\text{--}24^\circ$  landward, steeper than the interplate fault modeled in this study, possibly pointing to plate interface irregularities such as peaks of the oceanic relief. Occurrence of regular moderate size earthquakes would be consistent with sparse, kilometer-scale velocity weakening patches.
2. The LPI SSEs correlate spatially with the subducted oceanic relief (Figures 6 and 7), a similar observation as reported for other SSEs in Japan [*Kodaira et al.*, 2004] and New Zealand [*Bell et al.*, 2010; *Wallace et al.*, 2016]. According to their location proposed by *Chlieh et al.* [2014] and *Segovia et al.* [2015], the 2010 and 2013 SSEs occurred at least partly within the oceanic relief locked patch (Figures 3 and 6). SSEs documented so far are thought to initiate at transitions in frictional properties from unstable to stable sliding along the plate interface [*Schwartz and Rokosky*, 2007]. SSEs in the LPI area may reflect similar transitional friction areas interspersed between small-scale highly coupled patches.
3. The highly jagged interplate topography is assumed to be associated to a variable interplate fluid overpressure producing frictional anomalies that may contribute to the ISC heterogeneity [*Sage et al.*, 2006]. The peaks of the oceanic relief are inferred to locally increase the ISC, thus contributing to locking the plate interface, whereas the propagation of the 2013 SSE in between the peaks (Figures 3 and 6) denotes a potential weaker interplate contact. Shallow SSEs are believed to propagate within fluid-rich sediment identified along the plate interface in the vicinity of subducted seamounts [*Sage et al.*, 2006; *Bell et al.*, 2010]. Alternatively, since MCS data have not detected sediment on the subducted oceanic relief, the 2013 SSE may have propagated inside the base of the margin basement, along slip planes formed within a fluid-driven, long-term damaged zone [*Sage et al.*, 2006].

### 5.3. Potential Deformation of the Subducted Oceanic Relief

Seismic imaging has provided evidence that subducting seamounts survive to large depths, at least 10 km [*Kodaira et al.*, 2000; *Bangs et al.*, 2006; *Barker et al.*, 2009] and even to a depth of 30–40 km [*Singh et al.*, 2011]. However, as inferred from conceptual, numerical, and analog modeling, seamount likely deform during subduction and part of them may be sheared off as the seamount opposes substantial resistance to subduction [*Cloos*, 1992; *Dominguez et al.*, 1998; *Wang and Bilek*, 2011; *Bassett and Watts*, 2015; *Ruh et al.*, 2016]. Analyzing seismicity in the central Ecuador subduction zone suggests that the oceanic relief subducting beneath LPI is also deforming. Although fractured, the margin basement is not shattered as indicated by its remarkably high (5–6 km/s)  $V_p$  and should preserve some elastic properties. Earthquakes recorded by the Instituto Geofísico Escuela Politécnica Nacional (IG-EPN) local network (1994–2007) and

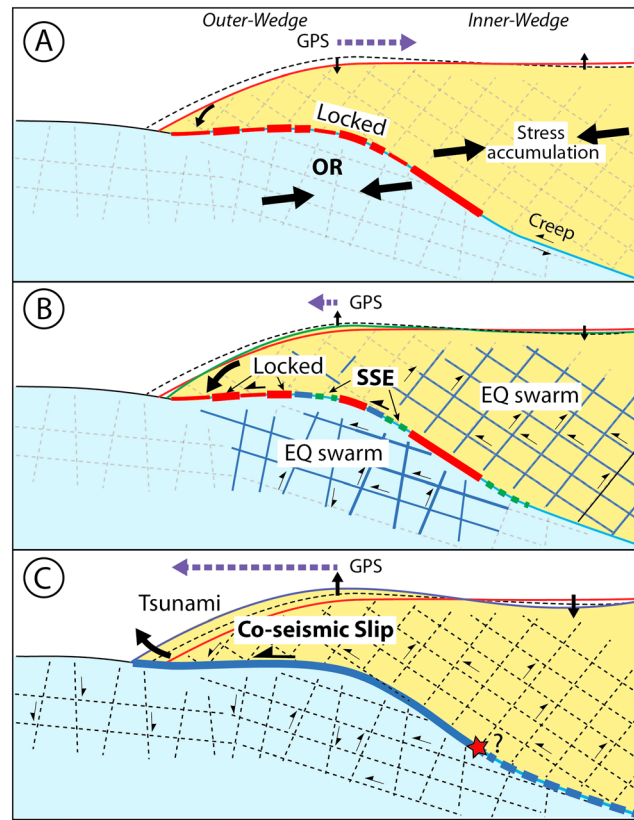


**Figure 9.** Synoptic model for shallow oceanic relief (OR) subduction over an earthquake cycle. (a) In a creeping subduction zone, stress accumulates as the plate interface locks at discrete peaks of the rugged topography of a subducted relief (thick red dashed curve); outer wedge subsides (thin red curve); the grey dashed mesh figures network of potential secondary faults. (b) Stress is partially released during slow slip events (SSEs) (green dashed lines), time-associated earthquake (EQ) swarms at the plate interface (thick blue dash), and at reactivated secondary faults (blue mesh), while patches of the oceanic relief keep remaining locked, outer wedge tilt increases seaward (thin green curve). Figures 9a and 9b repeat over time accommodating small steps of the oceanic relief subduction, possibly releasing most accumulated elastic strain. (c) Occasionally, if most elastic strain was not released over repeating Figures 9a and 9b, the entire updip megathrust (thick blue line) may unlock, generating a tsunamigenic/tsunami earthquake (red star). The black dashed mesh figures network of secondary faults potentially reactivated at this stage. Figure 9c has not been observed in the LPI region.

relocated by Font *et al.* [2013] attest that the margin crust inboard from the subducted oceanic relief is being pervasively fractured. However, aside from the  $M_w$  5.9–6.1 thrust events of the 2005 swarm [Vaca *et al.*, 2009] that likely occurred on the plate interface, most centroid moment tensor (CMT) focal mechanisms of the swarm largest events are poorly located in depth as explained by Ekström *et al.* [2012], and so poorly controlled is the depth of the seismicity relocated by Font *et al.* [2013], although these authors provided a theoretical average depth uncertainty of 1.4 km. Therefore, although some of these events could have ruptured the plate interface, others might have reactivated faults in both the margin basement and the subducting plate. This query can be partly addressed using seismological evidence that suggests that the subducting oceanic relief tectonically deforms during SSEs. The 2010 SSE time-related sharp increase in microseismicity [Vallée *et al.*, 2013] focused at 7–12 km depths and delineated a circular shape in map view (Figure 6), possibly outlining oceanic relief structures beneath the continental shelf. Even considering a  $\pm 2$  km depth uncertainty, most 2010 SSE seismicity occurs within the subducted relief (Figure 7). Such indication suggests that this seismicity does not identify the level of the current megathrust, but rather, secondary faults within the subducted relief, an outcome that markedly differs from the SSE seismicity location generally assumed to be adjacent [Sagiya, 2004; Delahaye *et al.*, 2009],

inside or very close to the SSE zone on the plate interface [Vallée *et al.*, 2013]. In our hypothesis, the stress increment induced by the SSE may have promoted seismic rupture on already near failure secondary faults within the subducted relief. It is noticeable that the 2010 SSE seismicity takes place in the highly reflective (DR reflectors; Figures 2 and 3), low- $V_p$  velocity zone (Figure 7) modeled from OBS data. This zone may feature a layer subject to mechanical weakness prone to deformation when stress episodically increases. Most of these earthquake thrust-motion-consistent polarities and waveforms [Vallée *et al.*, 2013] support contraction shearing within the stressed subducted relief. Although the total moment released by these earthquakes features  $<1\%$  of the moment liberated during the SSE [Vallée *et al.*, 2013], this process implies that the bulk of the subducted relief is being slowly dismembered along a newly forming detachment thrust or high-angle reverse faults. Such internal shearing might distribute the volume anomaly of the subducted relief over a wider area, thus contributing to reducing the magnitude of surface uplift above the subducted topography. In conclusion, as proposed by Watts *et al.* [2010], Wang and Bilek [2014], and Ruh *et al.* [2016], the subducted relief appears to overcome its geometrical resistance to fault motion by slowly shearing off part of it.

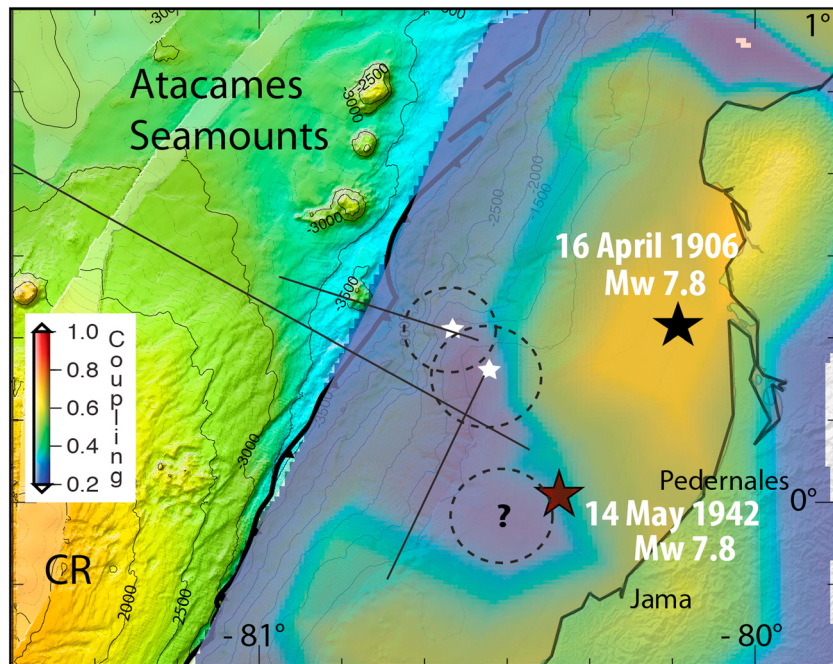


**Figure 10.** Subduction of the Atacames seamount chain beneath central Ecuador (modified from *Marcaillou et al.* [2016]); location is shown in Figure 1a; bathymetry is shown on the downgoing plate in meters with CR = Carnegie Ridge and ISC after [*Chlieh et al.*, 2014] on the upper plate; the white stars with dash circle indicate subducted seamounts identified on MCS lines (straight black lines). The large stars are 1942 and 2016 megathrust earthquake epicenters. Note that subducted seamount chain coincides with a low ISC area.

#### 5.4. Mode of Subduction of the Oceanic Relief and Seismic Potential

Because locked zones of the megathrust usually fail during large megathrust earthquakes, *Chlieh et al.* [2014] proposed that the size and level of ISC of the LPI asperity could host an  $M_w \sim 7.0\text{--}7.5$  earthquake. The observation of recurrent SSEs with slip located at least partly within the locked area found in this study suggests that some of the downdip progression of the oceanic relief takes place aseismically. SSE events with  $M_w$  equivalent to 6.0–6.3 or greater [*Vallée et al.*, 2013] and their associated  $M_w$  6.0+ earthquake swarms (Figure 7) together accommodate regular and localized small steps ( $\sim 50$  cm) of this progress. Longer observation time series are, however, required to evaluate the contribution of SSEs and seismic swarms to the slip budget. Although large earthquakes with  $M_w > 6.5$  have not been recorded in the LPI region, rupture of the LPI coupled patch during a larger event could not be ruled out. *Yang et al.* [2012] observe that a large earthquake may nucleate on a subducted seamount located at shallow depth.

Indeed, between successive SSEs and earthquake swarms, i.e., during periods of  $\sim 3\text{--}5$  years, the interplate segment located downdip and on either sides of the oceanic relief keeps creeping, so that the stiff part of the margin wedge remains stuck to the rugged oceanic relief surface, thus downflexing and storing elastic strain (Figure 9a). In this view, in complement to the oceanic relief small progresses during SSEs and their associated swarms (Figure 9b), substantial remaining elastic strain might ultimately be released on rare and larger seismic events causing a greater increment in the oceanic relief progress and potentially a tsunami (Figure 9c). Although not illustrated in LPI region, this possibility is substantiated at the Hikurangi margin, where a shallow, coupled subducted seamount associated with SSEs [*Bell et al.*, 2010; *Wallace et al.*, 2016] is believed to have produced the  $M_w$  6.9–7.1, 1947 tsunami earthquakes [*Bell et al.*, 2014].

#### 5.5. The Subducted Atacames Seamounts in Northern Ecuador

In contrast with the interplate locked patch associated to the subducted relief in the LPI region, the NS-trending Atacames seamount chain subducting beneath the North Ecuador margin correlates with a low ISC corridor [*Marcaillou et al.*, 2016]. However, due to a larger trench-coastline distance, a locked patch at the seamount scale may not be detected, as the ISC is less constrained near the trench in the Atacames seamount region, than in the LPI region [*Chlieh et al.*, 2014]. The corridor extends across the margin wedge

down to a series of locked patches [Chlieh *et al.*, 2014], two of them successively ruptured during the  $M_w$  7.8 2016 earthquake, in the same region as the preceding 1942  $M_w$  7.8 earthquake (Figure 10) [Nocquet *et al.*, 2016; Ye *et al.*, 2016].

Aside from their common erosive-type and mafic basement nature, the central and northern Ecuador subduction segments and their subducted oceanic reliefs show significant differences. The two subduction segments differ in stress environments, as a 7–8 km thick oceanic crust [Collot *et al.*, 2008; Marcaillou *et al.*, 2016] underthrusts obliquely the coupled northern segment, whereas the 14 km thick buoyant Carnegie Ridge [Graindorge *et al.*, 2004] underthrusts with low-obliquity the poorly coupled central segment. The Atacames seamounts have a higher (10–12%) height-to-width ratio, smaller 8–20 km diameter, 1–2 km high, with steeper slopes  $>20^\circ$  than the subducted oceanic relief in central Ecuador. Consequently, the north Ecuador margin wedge is deeply indented by the subducted seamounts and pervasively broken by intense reverse faulting, a process that is interpreted to have considerably lowered basement rock  $V_p$  velocity (3.5–4 km/s versus 4.5–5.5 km/s in the LPI region) and weakened the margin [Marcaillou *et al.*, 2016]. A 0.5–1.4 km thick subduction channel is imaged over the toe of the southern flank of the subducted Atacames seamount. Moreover, a seismically quiet zone overlaps the region of the subducted seamount chain, where no SSE has been documented yet. Marcaillou *et al.* [2016] speculate that the subducted Atacames seamounts stopped the updip propagation of the  $M_w$  7.8 1942 rupture according to the Yang *et al.* [2013] model, thus preventing tsunami generation, a situation that is similar to that observed at the erosive Japan margin, where  $M_w$  7.0 events have occurred in front of a weakly coupled, subducted seamount [Mochizuki *et al.*, 2008].

## 6. Conclusions

1. The combination of seismic imaging and new GPS data collected on La Plata Island and nearby Ecuadorian coastline sites shows that the oceanic relief subducted beneath La Plata Island is a locked asperity within the overall creeping subduction segment of the central Ecuador. Although nonunique, this result is rare with regard to the global compilation by Wang and Bilek [2014], which suggests that major subducted seamounts are predominantly associated with a creeping plate interface.
2. The subducted oceanic relief is viewed as a broad ( $\sim 55$  km  $\times$  50 km), sediment bare,  $\sim 1.5$ –2.0 km high, Carnegie Ridge basement rise studded with individual peaks. The oceanic relief that has a low height-to-width ratio and underthrusts a stiff, high- $V_p$  oceanic margin basement left subducted scars in the margin morphology and produced a late Pleistocene shelf basement flexural bulge that accounts for the recent LPI uplift.
3. The oceanic relief geometrical anomaly opposes a robust resistance to shear motion, indicated by the large-scale locked asperity in the ISC models. However, at a smaller scale, the fault friction within the locked asperity is suggested to be heterogeneous as both aseismic slip during SSEs and seismic slip during moderate size subduction earthquakes occur within the locked area, possibly reflecting different frictional properties at and in between the subducted peaks.
4. Small displacements along the interplate fault through frequent episodic SSE events and synchronous earthquake swarms predominantly accommodate the oceanic relief subduction. However, a larger event capable of rupturing the entire locked asperity and causing a larger increment in the oceanic relief progress is not to be excluded.
5. The oceanic relief geometrical resistance to subduction may result in the beginnings of shearing off a part of the oceanic relief as suggested by SSE-related microseismicity occurring within the subducted relief.
6. A comparison between the locked oceanic relief and the unlocked Atacames seamount chain both subducting beneath an erosive oceanic margin indicates that the subducted relief height-to-width ratio compared to the subduction channel thickness might play a major role on the local ISC. In absence of a detectable subduction channel, a broad, low height-to-width ratio, highly jagged oceanic relief subducted beneath a stiff margin basement would favor interplate coupling at the seamount scale, whereas the bulldozing effects of larger height-to-width ratio seamounts that fracture and weaken the margin would promote a weaker interplate coupling.
7. Because dense, near-trench geodetic measurements are still technically difficult, seismic imaging could be used as a proxy to constrain the near-trench subduction locking. Identifying the height-to-width ratio of shallow subducted oceanic reliefs relative to the thickness of the subduction channel at other subduction zones would help predicting areas of potential tsunamigenic earthquakes.

## Acknowledgments

This work was carried out in the frame of the Joint French-Ecuador Laboratory "Earthquakes and Volcanoes in the Northern Andes" and was funded by the Institut Français de Recherche pour le Développement (IRD), IFREMER, CNRS-INSU, and the Prometeo Project of the Ministry of Higher Education, Science, Technology and Innovation of the Republic of Ecuador. The data used are listed in the tables and supporting information. We thank B. Pontoise, Y. Hello, and N. Bethoux for the use of onshore-offshore wide-angle seismic data collected during the SISTEUR Project. Finally, we acknowledge J. Geersen, Emma Hill, and an anonymous reviewer for their helpful comments and J.-N. Proust for fruitful discussions. E. Sanclément acknowledges support provided by the IRD-DSF through a PhD grant.

## References

- Agudelo, W. (2005), Imagerie sismique quantitative de la marge convergente d'Equateur-Colombie, PhD thesis, 203 pp., Université Pierre et Marie Curie, Villefranche-sur-Mer.
- Agudelo, W., A. Ribodetti, J.-Y. Collot, and S. Operto (2009), Joint inversion of multichannel seismic reflection and wide-angle seismic data: Improved imaging and refined velocity model of the crustal structure of the north Ecuador-south Colombia convergent margin, *J. Geophys. Res.*, *114*, B02306, doi:10.1029/2008JB005690.
- Altamimi, Z., X. Collilieux, and L. Métivier (2011), ITRF2008: An improved solution of the international terrestrial reference frame, *J. Geod.*, *85*(8), 457–473.
- Al-Yahya, K. (1989), Velocity analysis by iterative profile migration, *Geophysics*, *54*, 718–729.
- Baldock, J. W. (1983), The northern Andes: A review of the Ecuadorian Pacific margin, in *The Ocean Basins and Margins—The Pacific Ocean*, edited by A. E. Nairn, F. G. Stehli, and S. Uyeda, pp. 181–217, Plenum Press, New York and London.
- Bangs, N. L. B., S. P. S. Gulick, and T. H. Shipley (2006), Seamount subduction erosion in the Nankai Trough and its potential impact on the seismogenic zone, *Geology*, *34*(8), 701–704, doi:10.1130/G22451.1.
- Barker, D. H. N., R. Sutherland, S. Henrys, and S. Bannister (2009), Geometry of the Hikurangi subduction thrust and upper plate, North Island, New Zealand, *Geochem. Geophys. Geosyst.*, *10*, Q02007, doi:10.1029/2008GC002153.
- Bassett, D., and A. B. Watts (2015), Gravity anomalies, crustal structure, and seismicity at subduction zones: 1. Seafloor roughness and subducting relief, *Geochem. Geophys. Geosyst.*, *16*, 1508–1540, doi:10.1002/2014GC005684.
- Beck, S. L., and L. J. Ruff (1984), The rupture process of the great 1979 Colombia earthquake: Evidence for the asperity model, *J. Geophys. Res.*, *89*, 9281–9291, doi:10.1029/JB089iB11p09281.
- Bell, R., R. Sutherland, D. H. N. Barker, S. Henrys, S. Bannister, L. Wallace, and J. Beavan (2010), Seismic reflection character of the Hikurangi subduction interface, New Zealand, in the region of repeated Gisborne slow slip events, *Geophys. J. Int.*, *180*, 34–48.
- Bell, R., C. Holden, W. Power, X. Wang, and G. Downes (2014), Hikurangi margin tsunami earthquake generated by slow seismic rupture over a subducted seamount, *Earth Planet. Sci. Lett.*, *397*, 1–9, doi:10.1016/j.epsl.2014.04.005.
- Bilek, S. L., S. Y. Schwartz, and H. R. DeShon (2003), Control of seafloor roughness on earthquake rupture behavior, *Geology*, *31*(5), 455–458.
- Blewitt, G., and D. Lavallée (2002), Effect of annual signals on geodetic velocity, *J. Geophys. Res.*, *107*(B7), 2145, doi:10.1029/2001JB000570.
- Cantalamesa, G., and C. Di Celma (2004), Origin and chronology of Pleistocene marine terraces of Isla de la Plata and of flat, gently dipping surfaces of the southern coast of Cabo San Lorenzo (Manabí, Ecuador), *J. South Am. Earth Sci.*, *16*, 633–648.
- Chlieh, M., et al. (2014), Distribution of discrete seismic asperities and aseismic slip along the Ecuadorian megathrust, *Earth Planet. Sci. Lett.*, *400*, 292–301, doi:10.1016/j.epsl.2014.05.027.
- Cloos, M. (1992), Thrust-type subduction-zone earthquakes and seamount asperities: A physical model for seismic rupture, *Geology*, *20*, 601–604.
- Collot, J.-Y., and M. A. Fisher (1989), Formation of forearc basins by collision between seamounts and accretionary wedges: An example from the New Hebrides subduction zone, *Geology*, *17*, 930–933.
- Collot, J.-Y., W. Agudelo, A. Ribodetti, and B. Marcaillou (2008), Origin of a crustal splay fault and its relation to the seismogenic zone and underplating at the erosional N-Ecuador S-Colombia oceanic margin, *J. Geophys. Res.*, *113*, B12102, doi:10.1029/2008JB005691.
- Cummins, P. R., T. Baba, S. Kodaira, and Y. Kaneda (2002), The 1946 Nankai earthquake and segmentation of the Nankai Trough, *Phys. Earth. Planet. Inter.*, *132*, 75–87.
- Delahaye, E. J., J. Townend, M. E. Reyners, and G. Rogers (2009), Microseismicity but no tremor accompanying slow slip in the Hikurangi subduction zone, New Zealand, *Earth Planet. Sci. Lett.*, *277*, 21–28, doi:10.1016/j.epsl.2008.09.038.
- Dominguez, S., S. Lallemand, J. Malavieille, and R. von Huene (1998), Upper plate deformation associated with seamount subduction, *Tectonophysics*, *293*, 207–224.
- Dominguez, S., J. Malavieille, and S. Lallemand (2000), Deformation of margins in response to seamount subduction insights from sandbox experiments, *Tectonics*, *19*(1), 182–196, doi:10.1029/1999TC900055.
- Duan, B. (2012), Dynamic rupture of the 2011  $M_w$  9.0 Tohoku-Oki earthquake: Roles of a possible subducting seamount, *J. Geophys. Res.*, *117*, B05311, doi:10.1029/2011JB009124.
- Ekström, G., M. Nettles, and A. M. Dziewonski (2012), The global CMT project 2004–2010: Centroid-moment tensors for 13,017 earthquakes, *Phys. Earth. Planet. Inter.*, *200–201*, 1–9.
- Fisher, M. A., J. Y. Collot, and E. L. Geist (1991), Structures of the collision zone between Bougainville Guyot and the accretionary wedge of the New Hebrides Island Arc, southwest Pacific, *Tectonics*, *10*, 887–903, doi:10.1029/91TC00860.
- Font, Y., M. Segovia, S. Vaca, and T. Theunissen (2013), Seismicity patterns along the Ecuadorian subduction zone: New constraints from earthquake location in a 3-D a priori velocity model, *Geophys. J. Int.*, *193*, 263–286, doi:10.1093/gji/ggs083.
- Gailler, A., P. Charvis, and E. R. Flueh (2007), Segmentation of the Nazca and South American plates along the Ecuador subduction zone from wide angle seismic profiles, *Earth Planet. Sci. Lett.*, *260*, 444–464, doi:10.1016/j.epsl.2007.05.045.
- Gansser, A. (1973), Facts and theories on the Andes, *J. Geol. Soc.*, *129*, 93–131.
- Geersen, J., C. R. Ranero, U. Barckhausen, and C. Reichert (2015), Subducting seamounts control interplate coupling and seismic rupture in the 2014 Iquique earthquake area, *Nat. Commun.*, doi:10.1038/ncomms9267.
- Gossens, P. J., and W. I. Rose (1973), Chemical composition and age determination of tholeiitic rocks in the basic igneous complex, Ecuador, *Geol. Soc. Am. Bull.*, *84*, 1043–1052.
- Graindorge, D., A. Calahorrano, P. Charvis, J.-Y. Collot, and N. Bethoux (2004), Deep structures of the Ecuador convergent margin and the Carnegie Ridge, possible consequence on great earthquakes recurrence interval, *Geophys. Res. Lett.*, *31*, L04603, doi:10.1029/2003GL018803.
- Hansen, P. C., and D. P. O'Leary (1993), The use of the L-curve in the regularization of discrete ill-posed problems, *SIAM J. Sci. Comput.*, *14*(6), 1487–1503.
- Hardy, N. C. (1991), Tectonic evolution of the easternmost Panama Basin: Some new data and inferences, *J. South Am. Earth Sci.*, *4*(3), 261–269.
- Hayes, G. P., D. J. Wald, and R. L. Johnson (2012), Slab1.0: A three-dimensional model of global subduction zone geometries, *J. Geophys. Res.*, *117*, B01302, doi:10.1029/2011JB008524.
- Herring, T. A., R. W. King, and S. C. McClusky (2010) *Documentation for the GAMIT/GLOBK Software Release 10.40*, pp. 1–171, Mass. Inst. of Technol., Cambridge.
- Hicks, S. P., A. Rietbrock, C. A. Haberland, I. M. A. Ryder, M. Simons, and A. Tassara (2012), The 2010  $M_w$  8.8 Maule, Chile earthquake: Nucleation and rupture propagation controlled by a subducted topographic high, *Geophys. Res. Lett.*, *39*, L19308, doi:10.1029/2012GL053184.

- Holtkamp, S. G., M. E. Pritchard, and M. E. Lohman (2011), Earthquake swarms in South America, *Geophys. J. Int.*, *187*, 128–146, doi:10.1111/j.1365-246X.2011.05137.x.
- Husen, S., E. Kissling, and R. Quintero (2002), Tomographic evidence for a subducted seamount beneath the Gulf of Nicoya, Costa Rica: The cause of the 1990  $M_w = 7.0$  Gulf of Nicoya earthquake, *Geophys. Res. Lett.*, *29*(8), 1238, doi:10.1029/2001GL014045.
- Kanamori, H., and K. C. McNally (1982), Variable rupture mode of the subduction zone along the Ecuador-Colombia coast, *Bull. Seismol. Soc. Am.*, *72*(4), 1241–1253.
- Kelleher, J. (1972), Rupture zones of large South American earthquakes and some predictions, *J. Geophys. Res.*, *77*, 2087–2103, doi:10.1029/JB077i011p02087.
- Kelleher, J., and W. McCann (1976), Buoyant zones, great earthquakes, and unstable boundaries of subduction, *J. Geophys. Res.*, *81*(26), 4885–4896, doi:10.1029/JB081i026p04885.
- Kodaira, S., N. Takahashi, A. Nakanishi, S. Miura, and Y. Kaneda (2000), Subducted seamount imaged in the rupture zone of the 1946 Nankaido earthquake, *Science*, *289*, 104–106.
- Kodaira, S., T. Likada, A. Kato, J.-O. Park, T. Iwasaki, and Y. Kaneda (2004), High pore fluid pressure may cause silent slip in the Nankai Trough, *Science*, *304*, 1295–1298.
- Kyriakopoulos, C., and A. V. Newman (2016), Structural asperity focusing locking and earthquake slip along the Nicoya megathrust, Costa Rica, *J. Geophys. Res. Solid Earth*, *121*, 5461–5476, doi:10.1002/2016JB012886.
- Lallemant, S. E., and X. Le Pichon (1987), Coulomb wedge model applied to subduction of seamounts in the Japan Trench, *Geology*, *15*, 1065–1069.
- Lines, L. (1993), Ambiguity in analysis of velocity and depth, *Geophysics*, *58*, 596–597.
- Lonsdale, P. (1978), Ecuadorian subduction system, *Am. Assoc. Pet. Geol. Bull.*, *62*(12), 2454–2477.
- Lonsdale, P., and K. D. Klitgord (1978), Structure and tectonic history of the eastern Panama Basin, *Geol. Soc. Am. Bull.*, *89*, 981–999.
- Loveless, J. P., and B. J. Meade (2011), Spatial correlation of interseismic coupling and coseismic rupture extent of the 2011  $M_w = 9.0$  Tohoku-oki earthquake, *Geophys. Res. Lett.*, *38*, L17306, doi:10.1029/2011GL048561.
- Marcaillou, B., J.-Y. Collot, A. Ribodetti, E. d'Acromont, A.-A. Mahamat, and A. Alvarado (2016), Seamount subduction at the north-Ecuadorian convergent margin: Effects on structures, inter-seismic coupling and seismogenesis, *Earth Planet. Sci. Lett.*, *433*, 146–158.
- Martillo, C., J.-N. Proust, F. Michaud, and J.-Y. Collot (2013), Pleistocene stratigraphic signature of active deformation along the central Ecuadorian subduction margin, paper presented at 14<sup>th</sup> Congrès Français de Sédimentologie, Association des sédimentologues français, Paris, 4–8 Nov.
- McIntosh, K. D., E. A. Silver, I. Ahmed, A. Berhorst, C. R. Ranero, K. Kelly, and E. R. Flueh (2007), The Nicaragua convergent margin, seismic reflection imaging of the source of a tsunami earthquake, in *The Seismogenic Zone of Subduction Thrust Faults*, edited by T. H. Dixon and J. C. Moore, pp. 257–287, Colombia Univ. Press, New York.
- Michaud, F., J.-Y. Collot, A. Alvarado, E. López y el personal científico y técnico del INOCAR (2006), República del Ecuador, Batimetría y Relieve Continental, INOCAR, IOA-CVM-02-Post, Quito, Ecuador.
- Mochizuki, K., T. Yamada, M. Shinohara, Y. Yamanaka, and T. Kanazawa (2008), Weak interplate coupling by seamounts and repeating  $M=7$  earthquakes, *Science*, *321*, 1194–1197, doi:10.1126/science.1160250.
- Mothes, P., J.-M. Nocquet, and P. Jarrin (2013), Continuous GPS network operating throughout Ecuador, *Eos Trans. AGU*, *94*(26), 229–231.
- Nocquet, J.-M., et al. (2014), Motion of continental slivers and creeping subduction in the northern Andes, *Nat. Geosci.*, *1-5*, doi:10.1038/NGEO2099.
- Nocquet, J.-M., et al. (2016), Supercycle at the Ecuadorian subduction zone revealed after the 2016 Pedernales earthquake, *Nat. Geosci.*, doi:10.1038/NGEO2864.
- Oakley, A. J., B. Taylor, and G. F. Moore (2008), Pacific Plate subduction beneath the central Mariana and Izu-Bonin fore arcs: New insights from an old margin, *Geochem. Geophys. Geosyst.*, *9*, Q06003, doi:10.1029/2007GC001820.
- Okada, Y. (1992), Internal deformation due to shear and tensile faults in a half-space, *Bull. Seismol. Soc. Am.*, *82*, 1018–1040.
- Park, J.-O., T. Tsuru, Y. Kaneda, and Y. Kono (1999), A subducting seamount beneath the Nankai accretionary prism off Shikoku, southwestern Japan, *Geophys. Res. Lett.*, *26*(7), 931–934, doi:10.1029/1999GL900134.
- Pedroja, K., L. Ortlieb, J. F. Dumont, M. Lamothe, B. Ghaleb, M. Auclair, and B. Labrousse (2006), Quaternary coastal uplift along the Talara Arc (Ecuador, northern Peru) from new marine terrace data, *Mar. Geol.*, *228*, 73–91.
- Pennington, W. D. (1981), Subduction of the eastern Panama Basin and seismotectonics of northwestern South America, *J. Geophys. Res.*, *86*, 10,753–10,770, doi:10.1029/JB086iB11p10753.
- Perfettini, H., et al. (2010), Seismic and aseismic slip on the Central Peru megathrust, *Nature*, *465*, 78–81, doi:10.1038/nature09062.
- Proust, J.-N., C. Martillo, F. Michaud, J.-Y. Collot, and O. Dauteuil (2016), Subduction of seafloor asperities revealed by a detailed stratigraphic analysis of the active margin shelf sediments of central Ecuador, *Mar. Geol.*, *380*, 345–362, doi:10.1016/j.margeo.2016.03.014.
- Radiguet, M., F. Cotton, M. Vergnolle, M. Campillo, A. Walpersdorf, N. Cotte, and V. Kostoglodov (2012), Slow slip events and strain accumulation in the Guerrero gap, Mexico, *J. Geophys. Res.*, *117*, B04305, doi:10.1029/2011JB008801.
- Reynaud, C., E. Jaillard, H. Lapierre, M. Mamberti, and G. H. Mascle (1999), Oceanic plateau and island arcs of southwestern Ecuador: Their place in the geodynamic evolution of northwestern South America, *Tectonophysics*, *307*, 235–254.
- Ross, W. S. (1994), The velocity-depth ambiguity in seismic traveltimes data, *Geophysics*, *59*, 830–843.
- Ruh, J. B., V. Sallarès, C. R. Ranero, and T. Gerya (2016), Crustal deformation dynamics and stress evolution during seamount subduction: High-resolution 3-D numerical modeling, *J. Geophys. Res. Solid Earth*, *121*, 6880–6902, doi:10.1002/2016JB013250.
- Sage, F., J.-Y. Collot, and C. R. Ranero (2006), Interplate patchiness and subduction-erosion mechanisms: Evidence from depth migrated seismic images at the central Ecuador convergent margin, *Geology*, *34*(12), 997–1000, doi:10.1130/G22790A.1.
- Sagiya, T. (2004), Interplate coupling in the Kanto district, central Japan, and the Boso Peninsula silent earthquake in May 1996, *PAGEOPH*, *161*(11–12), 2327–2342, doi:10.1007/s00024-004-2566-6.
- Sallares, V., and P. Charvis (2003), Crustal thickness constraints on the geodynamic evolution of the Galapagos Volcanic Province, *Earth Planet. Sci. Lett.*, *214*, 545–559.
- Savage, J. C. (1983), A dislocation model of strain accumulation and release at a subduction zone, *J. Geophys. Res.*, *88*, 4984–4996, doi:10.1029/JB088iB06p04984.
- Scholz, C. H., and C. Small (1997), The effect of seamount subduction on seismic coupling, *Geology*, *25*, 487–490.
- Schwartz, S. Y., and J. M. Rokosky (2007), Slow slip events and seismic tremor at circum-pacific subduction zones, *Rev. Geophys.*, *45*, RG3004, doi:10.1029/2006RG000208.
- Segovia, M., Y. Font, M. Régnier, P. Charvis, J.-M. Nocquet, A. Galve, Y. Hello, A. Ogé, P. Jarrin, and M. Ruiz (2015), Intense microseismicity associated with a SSE at La Plata Island in the central subduction zone of Ecuador, Abstract S31A-2736 presented at 2015 Fall Meeting, AGU, San Francisco, Calif., 14–18 Dec.

- Singh, S. C., et al. (2011), Aseismic zone and earthquake segmentation associated with a deep subducted seamount in Sumatra, *Nat. Geosci.*, *4*, 308–311, doi:10.1038/NGEO1119.
- Sparkes, R., F. Tilmann, N. Hovius, and J. Hillier (2010), Subducted seafloor relief stops rupture in South American great earthquakes: Implications for rupture behaviour in the 2010 Maule, Chile earthquake, *Earth Planet. Sci. Lett.*, *298*, 89–94, doi:10.1016/j.epsl.2010.07.029.
- Stark, P. B., and R. L. Parker (1995), Bounded-variable least-squares: An algorithm and applications, *Comput. Stat.*, *10*, 129–129.
- Tarantola, A. (2005), *Inverse Problem Theory and Methods for Model Parameter Estimation*, 333 pp., Society for Industrial and Applied Mathematics, Philadelphia, Pa.
- Taylor, F. W., et al. (2005), Rapid forearc uplift and subsidence caused by impinging bathymetric features: Examples from the New Hebrides and Solomon arcs, *Tectonics*, *24*, TC6005, doi:10.1029/2004TC001650.
- Thierry, P., S. Operto, and G. Lambaré (1999), Fast 2-D ray + born inversion/migration in complex media, *Geophysics*, *64*, 162–181, doi:10.1190/1191.1444513.
- Vaca, S., M. Régnier, N. Bethoux, V. Alvarez, and B. Pontoise (2009), Sismicidad de la region de Manta: Enjambre sísmico de Manta-2005, in *Geología y Geofísica Marina y Terrestre del Ecuador: Desde la Costa Continental Hasta las Islas Galápagos*, edited by J.-Y. Collot, V. Sallares, and N. Pazmino, pp. 151–166, CNDM; IRD; INOCAR, Guayaquil, Ecuador.
- Vallée, M., et al. (2013), Intense interface seismicity triggered by a shallow slow slip event in the central Ecuador subduction zone, *J. Geophys. Res. Solid Earth*, *118*, 1–17, doi:10.1002/jgrb.50216.
- von Huene, R., C. R. Ranero, W. Weinrebe, and K. Hinz (2000), Quaternary convergent margin tectonics of Costa Rica, segmentation of the Cocos Plate and Central American volcanism, *Tectonics*, *19*(2), 314–334, doi:10.1029/1999TC001143.
- von Huene, R., C. R. Ranero, and P. Vannucchi (2004), Generic model of subduction erosion, *Geology*, *32*(10), 913–916.
- Wallace, L. M., et al. (2009), Characterizing the seismogenic zone of a major plate boundary subduction thrust: Hikurangi margin, New Zealand, *Geochem. Geophys. Geosyst.*, *10*, Q10006, doi:10.1029/2009GC002610.
- Wallace, L. M., S. C. Webb, Y. Ito, K. Mochizuki, R. Hino, S. Henrys, S. Y. Schwartz, and A. F. Sheehan (2016), Slow slip near the trench at the Hikurangi subduction zone, New Zealand, *Science*, *352*(6286), 701–704, doi:10.1126/science.aaf2349.
- Wang, K., and S. L. Bilek (2011), Do subducting seamounts generate or stop large earthquakes?, *Geology*, *39*(9), 819–822, doi:10.1130/G31856.1.
- Wang, K., and S. L. Bilek (2014), Invited review paper: Fault creep caused by subduction of rough seafloor relief, *Tectonophysics*, *610*, 1–24, doi:10.1016/j.tecto.2013.11.024.
- Wang, K., and T. Dixon (2004), “Coupling” semantics and Science in earthquake research, *Eos Trans. AGU*, *85*(18), 179–180.
- Watts, A. B., A. A. P. Koppers, and D. P. Robinson (2010), Seamount subduction and earthquakes, *Oceanography*, *23*(1), 166–173.
- Williams, S. P. (2008), CATS: GPS coordinate time series analysis software, *GPS Solutions*, *2*(2), 147–153, doi:10.1007/s10291-007-0086-4.
- Yang, H., Y. Liu, and J. Lin (2012), Effects of subducted seamounts on megathrust earthquake nucleation and rupture propagation, *Geophys. Res. Lett.*, *39*, L24302, doi:10.1029/2012GL053892.
- Yang, H., Y. Liu, and J. Lin (2013), Geometrical effects of a subducted seamount on stopping megathrust ruptures, *Geophys. Res. Lett.*, *40*, 2011–2016, doi:10.1002/grl.50509.
- Ye, A., H. Kanamori, J.-P. Avouac, L. Li, K. Fai Cheung, and T. Lay (2016), The 16 April 2016,  $M_w7.8$  ( $M_57.5$ ) Ecuador earthquake: A quasi-repeat of the 1942  $M_57.5$  earthquake and partial re-rupture of the 1906  $M_58.6$  Colombia-Ecuador earthquake, *Earth Planet. Sci. Lett.*, *454*, 248–258.
- Yepes, H., L. Audin, A. Alvarado, C. Beauval, J. Aguilar, Y. Font, and F. Cotton (2016), A new view for the geodynamics of Ecuador: Implication in seismogenic source definition and seismic hazard assessment, *Tectonics*, *35*, 1249–1279, doi:10.1002/2015TC003941.
- Zelt, C. A., and R. B. Smith (1992), Seismic traveltime inversion for 2-D crustal velocity structure, *Geophys. J. Int.*, *108*, 16–34.